

HST/COS OBSERVATIONS OF QUASAR OUTFLOWS IN THE 500 – 1050 Å REST-FRAME: II THE MOST ENERGETIC QUASAR OUTFLOW MEASURED TO DATE

XINFENG XU^{1,†}, NAHUM ARAV¹, TIMOTHY MILLER¹, GERARD A. KRISS², RACHEL PLESHA²

¹Department of Physics, Virginia Tech, Blacksburg, VA 24061, USA

²Space Telescope Science Institute, 3700 San Martin Drive, Baltimore, MD 21218, USA

Submitted to ApJS 2019 Jul 14; Accepted 2019 Sep 24

ABSTRACT

We present a study of the BAL outflows seen in quasar SDSS J1042+1646 ($z = 0.978$) in the rest-frame 500 – 1050 Å (EUV500) region. The results are based on the analysis of recent *Hubble Space Telescope/Cosmic Origins Spectrograph* observations. Five outflow systems are identified, where in total they include ~ 70 outflow troughs from ionic transitions. These include the first non-solar detections from transitions of O v*, Ne v*, Ar vi, Ca vi, Ca vii, and Ca viii. The appearance of very high-ionization species (e.g., Ne viii, Na ix, and Mg x) in all outflows necessitates at least two-ionization phases for the observed outflows. We develop an interactive Synthetic Spectral Simulation method to fit the multitude of observed troughs. Detections of density sensitive troughs (e.g., Si iv* $\lambda 657.32$ Å and the O v* multiplet) allow us to determine the distance of the outflows (R) as well as their energetics. Two of the outflows are at $R \simeq 800$ pc and one is at $R \simeq 15$ pc. One of the outflows has the highest kinetic luminosity on record ($\dot{E}_k = 5 \times 10^{46}$ erg s⁻¹), which is 20% of its Eddington luminosity. Such a large ratio suggests that this outflow can provide the energy needed for active galactic nucleus feedback mechanisms.

Keywords: galaxies: active – galaxies: kinematics and dynamics – quasars: jets and outflows – quasars: absorption lines – quasars: general – quasars: individual (SDSS J1042+1646)

1. INTRODUCTION

Quasar absorption outflows are identified by blue-shifted troughs that appear in quasar spectra (e.g., Hall et al. 2002; Arav et al. 2013; Grier et al. 2015; Leighly et al. 2018; Hamann et al. 2019). These outflows are believed to play a major role in various active galactic nucleus (AGN) feedback mechanisms (see elaboration in section 1 of Arav et al. 2019, submitted to ApJS, hereafter Paper I). Observations and analyses show that these outflows can have enough kinetic energy to be major contributors to AGN feedback (e.g., Moe et al. 2009; Dunn et al. 2010; Borguet et al. 2013; Arav et al. 2013; Chamberlain & Arav 2015; Xu et al. 2019a). To assess how effective outflows are at contributing to AGN feedback, theoretical models compare the kinetic luminosity of the outflow (\dot{E}_k) to the Eddington luminosity of the central black hole (L_{Edd}). These models predict that an Eddington ratio, i.e., $\Gamma_{\text{Edd}} \equiv \dot{E}_k/L_{\text{Edd}}$, of at least 0.5 – 5% is required for strong AGN feedback effects (Hopkins & Elvis 2010; Scannapieco & Oh 2004, respectively).

Broad absorption line quasars (BALQSOs) are observed in $\simeq 20\%$ of the optically selected quasar population (e.g., Hall et al. 2002; Tolea et al. 2002; Hewett & Foltz 2003; Reichard et al. 2003; Trump et al. 2006; Ganguly & Brotherton 2008; Gibson et al. 2009, and references therein). The majority of observed BALQSOs only show absorption troughs from high-ionization species, e.g., C iv, N v, Si iv (and H i), and are designated as HiBALs. There are more than 10,000 ground-based spectra of such outflows. However, almost all of these cover rest-frame wavelengths longer than 1050 Å (Arav et al. 2013). For these wavelengths, it is very rare to find

diagnostic troughs that allow distance measurements of the outflow from the central source (R) (e.g., Hamann 1998; Borguet et al. 2012b, 2013; Capellupo et al. 2014, 2017; Arav et al. 2018; Xu et al. 2019a). Furthermore, the $\lambda_{\text{rest}} > 1050$ Å cannot probe the very-high ionization phase (VHP, probed by troughs from Ne viii, Mg x, Si xii, and higher-ionization species). The VHP has been shown to carry more than 90% of the outflow's total hydrogen column density (N_{H}) both in X-ray spectra of Seyfert outflows (e.g., Behar et al. 2017) as well as in quasar outflows where troughs from the above species were covered (Arav et al. 2013; Finn et al. 2014). These two parameters (R and N_{H}) are the key to determining \dot{E}_k (see equation (5)) and, therefore, the possible contribution of the outflow to AGN feedback.

The 500 – 1050 Å rest-frame region (hereafter EUV500) contains 10 times more measurable absorption features in a quasar outflow (Arav et al. 2013). Some of these have been observed and reported, including transitions from N iv, O iv, O iv*, O v, O vi, Ne iv, Ne v, Ne vi, Ne viii, Na ix, Mg x, Al xi, Si xii, S v, Ar vii, and Ar viii (see table 3 for details of the specific transitions; Korista et al. 1992; Telfer et al. 1998, 2002; Arav et al. 2001; Muzahid et al. 2013; Finn et al. 2014). These include troughs from the very-high ionization phase, which can be used to determine N_{H} (Arav et al. 2013), and troughs from more than 10 excited state transitions, which can be used to determine the electron number density (n_e) of an outflow and therefore R (e.g., Hamann et al. 2001; Borguet et al. 2012a; Xu et al. 2018, 2019a). Here we report the first non-solar detection of troughs from O v*, Ne v*, Ar vi, Ca vi, Ca vii, and Ca viii (see table 3 for details).

We carried out a *Hubble Space Telescope* (HST)

[†] Email: xinfeng@vt.edu

program GO 14777 (PI: Arav), which targeted a sample of 10 quasars (see selection criteria in Arav et al. 2019, submitted) and observed the EUV500 with the *Cosmic Origins Spectrograph* (COS). Using HST is necessary since observing the EUV500 with ground-based telescopes requires objects with redshift, $z \gtrsim 3$. At these redshifts, the contamination from the Ly α forest is severe, which does not allow for adequate measurements of EUV500 troughs and, in most cases, not even their detections. Therefore, the EUV500 is only practicably accessible with the HST by observing bright quasars at $0.5 \lesssim z \lesssim 2$ (Korista et al. 1992; Arav et al. 1999; Telfer et al. 2002; Arav et al. 2001, 2013; Finn et al. 2014).

This paper is part of a series of publications describing the results of HST program GO-14777, which observed quasar outflows in the EUV500 using the COS.

Paper I (Arav et al. 2020) summarizes the results for the individual objects and discusses their importance to various aspects of quasar outflow research.

Paper II is this work.

Paper III (Miller et al. 2020a) analyzes 4 outflows detected in 2MASS J1051+1247, which show remarkable similarities, are situated at $R \sim 200$ pc and have a combined $\dot{E}_k = 10^{46}$ erg s $^{-1}$.

Paper IV (Xu et al. 2020b) presents the largest velocity shift and acceleration measured to date in a BAL outflow.

Paper V (Miller et al. 2020b) analyzes 2 outflows detected in PKS 0352-0711, one outflow at $R = 500$ pc and a second outflow at $R = 10$ pc that shows an ionization potential-dependent velocity shift for troughs from different ions.

Paper VI (Xu et al. 2020c) analyzes 2 outflows detected in SDSS 0755+2306, including one at $R = 1600$ pc with $\dot{E}_k = 10^{46} - 10^{47}$ erg s $^{-1}$.

Paper VII (Miller et al. 2020c) discusses the other objects observed by program GO-14777, whose outflow characteristics make the analysis more challenging.

In this paper, we describe the analysis of outflows seen in quasar SDSS J1042+1646. The structure of the paper is as follows. In section 2, we discuss the details of the observations and data reductions. In section 3, we introduce our spectral analysis method. We present the analysis of each outflow system in section 4, where the photoionization solutions and n_e are determined. In section 5, we determine the distances and energetics for the outflows, and discuss these results in section 6. We summarize the paper in section 7. We adopt a cosmology with $H_0 = 69.6$ km s $^{-1}$ Mpc $^{-1}$, $\Omega_m = 0.286$, and $\Omega_\Lambda = 0.714$, and we use Ned Wright’s Javascript Cosmology Calculator website (Wright 2006).

2. OBSERVATIONS AND DATA REDUCTION

SDSS J1042+1646 (J2000: R.A. = 10:42:44.24, decl. = +16:46:56.14, $z = 0.978$) was observed with HST/COS (Green et al. 2012) in November 2017 as part of our HST/COS program GO 14777 (PI: Arav). We used the G130M and G160M gratings, which have a resolving power of $\lambda/\delta\lambda \simeq 12,000 - 17,000$ and $14,000 - 19,000$, respectively (Fox, et al. 2018). Our G130M observations cover the wavelength range of 1132 – 1472 Å and

Table 1
HST/COS Observations for SDSS J1042+1646

Epoch	Date	Exp.(s)	Grating
1	2017 Nov 13, 18:20:01	1720	G130M
2	2017 Nov 13, 19:44:17	1640	G130M
3	2017 Nov 13, 21:08:53	2320	G160M
4	2017 Nov 13, 22:46:04	2600	G160M
5	2011 Jun 15, 19:17:32	900	G140L

Table 2
Outflows Detected in the SDSS J1042+1646 Data

Outflow System	Velocity ^a (km s $^{-1}$)	Ne VIII Abs. Width ^b (km s $^{-1}$)
S1	-5300	2500
S2	-7500	1500
S3	-9940	1350
S4, 2011	-19500	2000
S4, 2017	-21050	2000

Note. —

^a The velocity centroids come from the Gaussian profile fitting to unblended absorption troughs, e.g., Ar VIII $\lambda\lambda 700.24, 713.80$.

^b Ne VIII $\lambda 770.41$ absorption trough width is measured for continuous absorption below the normalized flux $I = 0.9$

the G160M ones cover 1383 – 1801 Å in the observed-frame. This object was observed previously in June 2011 using HST/COS G140L in program GO 12289 (PI: J. Howk). The COS G140L has a wider spectral coverage, 1100 – 2000 Å and lower resolving power $\sim 1500 - 4000$. There is a spectral gap in the G140L grating from around 1153 Å to 1185 Å. We show the details of both datasets in table 1.

We reduced the SDSS J1042+1646 data and estimated the errors following the same procedure described in Miller et al. (2018). For the 2017 observations, we combined the two observations for each grating. We corrected for Galactic extinction with $E(B-V) = 0.022$ (Schlafly & Finkbeiner 2011). We show the full, dereddened spectrum in figure 1.

3. SPECTRAL ANALYSIS

3.1. Unabsorbed Emission Model

We model the unabsorbed emission of the two different epochs separately following the approach of Chamberlain & Arav (2015); Miller et al. (2018); Xu et al. (2018). The models include two components: 1) a continuum which is represented by a power law; 2) strong emission lines such as O V and Ne VIII, which are fitted with one or more Gaussian profiles. The adopted emission model for the 2017 epoch is shown as the solid red line in figure 1.

3.2. Identifying Outflow Systems

The COS EUV500 spectrum of SDSS J1042+1646 shows a variety of absorption features due to the interstellar medium (ISM) within our galaxy, intervening Ly α forest systems, and quasar outflow absorption features at different velocities. We identify five kinematically distinct outflow systems (S1 – S4, where S1 has two components: S1a and S1b, see table 2). The full, dereddened

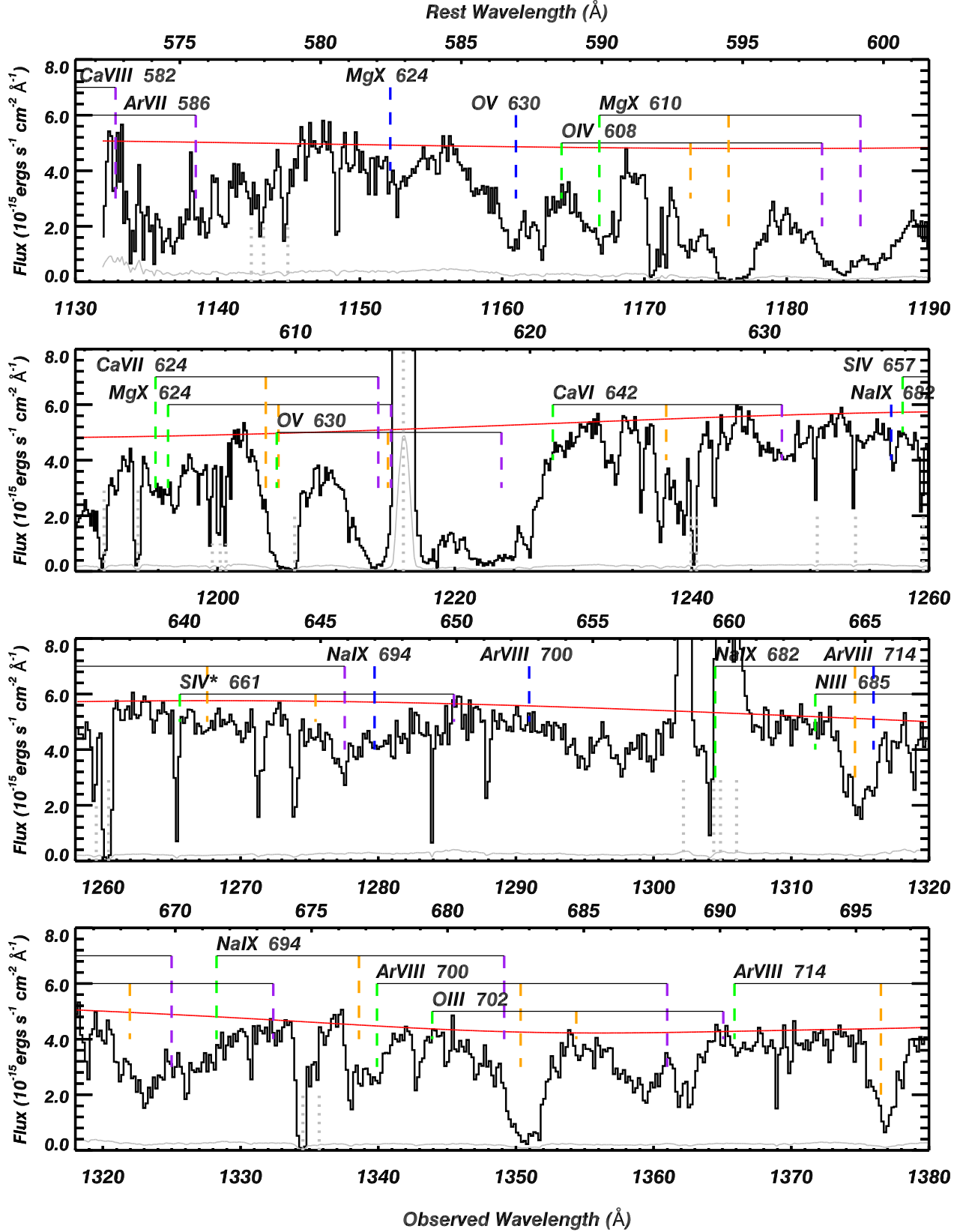


Figure 1. HST/COS dereddened spectrum of SDSS J1042+1646 ($z = 0.978$). The black histogram shows the data from the 2017 epoch. The unabsorbed emission model and the flux error are shown as the red and gray solid lines, respectively. We label the important ionic absorption troughs in order of increasing velocity offset for all 5 outflow systems (see section 4) with purple (S1a and S1b), orange (S2), green (S3), and blue (S4) vertical dashed lines. Strong Galactic ISM lines (e.g., Si II at 1260.42 Å) and geocoronal lines (e.g., H I at 1215.67 Å , O I at 1302.17 Å , and O I* at 1304.86 Å , 1306.03 Å) are marked with gray dotted lines under the spectrum.

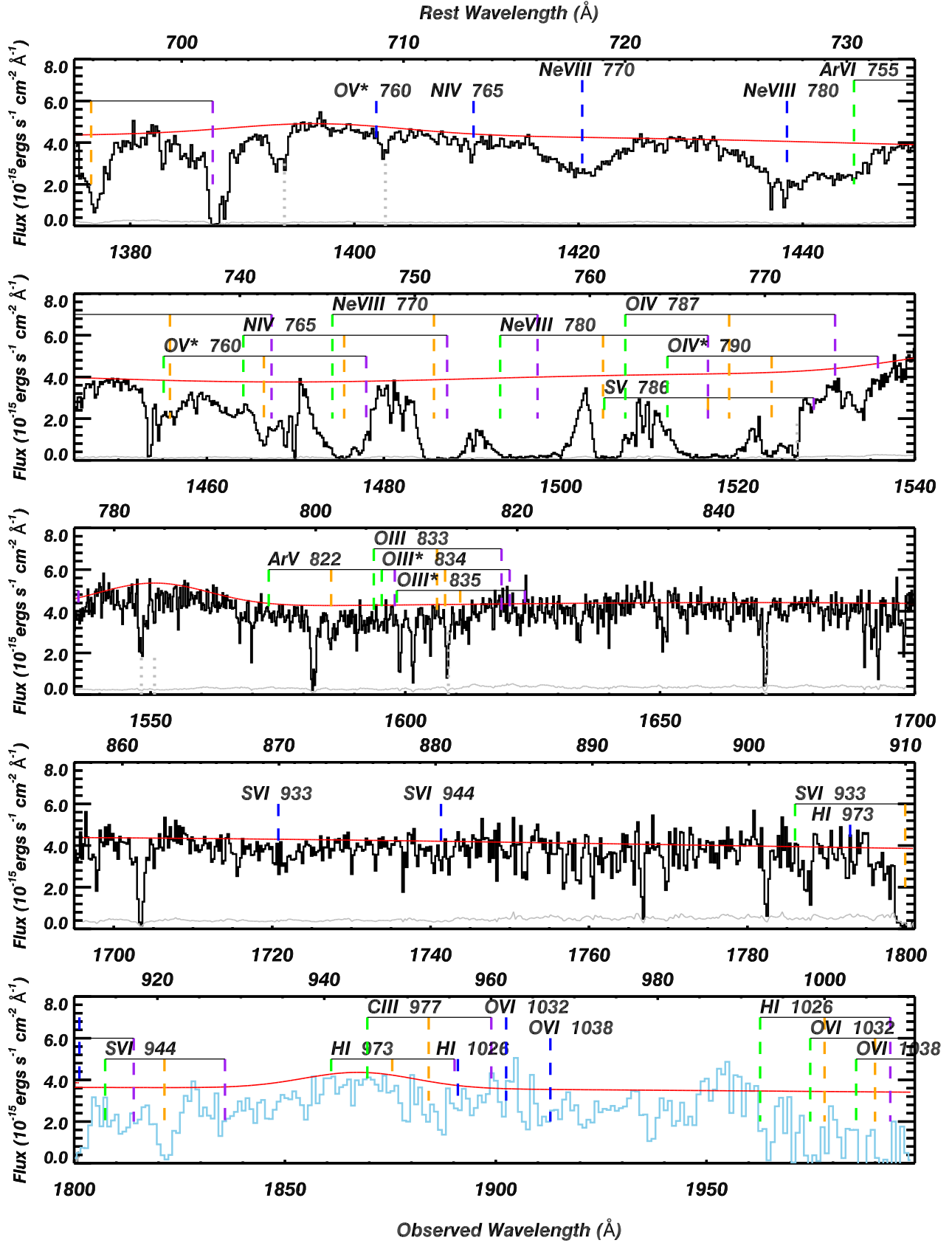


Table 3
Atomic Data for Observed Transitions in EUV500 Range

Ion ⁽¹⁾	$\lambda^{(2)}$ (Å)	$E_{low}^{(3)}$ (cm ⁻¹)	$f^{(4)}$	IP ⁽⁵⁾ (eV)	$\log(n_{e,crit})^{(6)}$ log(cm ⁻³)
H I	937.803	0.00	0.008	13.60	—
H I	949.743	0.00	0.014	13.60	—
H I ⁽⁷⁾	972.537	0.00	0.029	13.60	—
H I	1025.72	0.00	0.079	13.60	—
C III	977.020	0.00	0.759	47.89	—
N III	684.998	0.00	0.135	47.45	—
N III	685.515	0.00	0.270	47.45	—
N III*	685.817	174.4	0.320	47.45	3.3
N III*	686.336	174.4	0.069	47.45	3.3
N III	763.334	0.00	0.084	47.45	—
N III*	764.351	174.4	0.081	47.45	3.3
N III	989.799	0.00	0.123	47.45	—
N III*	991.511	174.4	0.122	47.45	3.3
N IV	765.147	0.00	0.611	77.47	—
O III*	599.590	20273.27	0.292	77.47	5.9
O III	702.337	0.00	0.134	54.93	—
O III*	702.900	113.2	0.135	54.93	3.1
O III*	703.854	306.2	0.136	54.93	3.7
O III	832.929	0.00	0.106	54.93	—
O III*	833.749	113.2	0.106	54.93	3.1
O III*	835.289	306.2	0.104	54.93	3.7
O IV	608.397	0.00	0.067	77.41	—
O IV*	609.829	385.9	0.067	77.41	4.1
O IV	787.710	0.00	0.111	77.41	—
O IV*	790.199	385.9	0.110	77.41	4.1
O V	629.732	0.00	0.512	113.90	—
O V* J=1	758.677	82078.6	0.080	113.90	— ⁽⁸⁾
O V* J=0	759.442	81942.5	0.191	113.90	—
O V* J=1	760.227	82078.6	0.048	113.90	—
O V* J=2	760.446	82385.3	0.143	113.90	—
O V* J=1	761.128	82078.6	0.064	113.90	—
O V* J=2	762.004	82385.3	0.048	113.90	—
O VI	1031.912	0.00	0.133	138.12	—
O VI	1037.613	0.00	0.066	138.12	—
Ne IV	541.128	0.00	0.055	97.11	—
Ne IV	542.074	0.00	0.110	97.11	—
Ne IV	543.884	0.00	0.170	97.11	—
Ne V	568.424	0.00	0.110	126.21	—
Ne V*	569.828	411.2	0.109	126.21	4.3
Ne V*	572.335	1109.5	0.114	126.21	4.9
Ne VI	558.603	0.00	0.092	157.93	—
Ne VIII	770.409	0.00	0.102	239.09	—
Ne VIII	780.324	0.00	0.050	239.09	—
Na IX	681.720	0.00	0.092	299.90	—
Na IX	694.150	0.00	0.045	299.90	—
Mg X	609.793	0.00	0.084	367.50	—
Mg X	624.941	0.00	0.041	367.50	—
Al XI	550.030	0.00	0.077	442.00	—
Al XI	568.120	0.00	0.037	442.00	—
Si XII	499.406	0.00	0.072	523.00	—
Si XII	520.665	0.00	0.034	523.00	—
S IV	657.319	0.00	1.130	47.30	—
S IV*	661.396	951.4	1.020	47.30	4.8
S IV*	661.455	951.4	0.118	47.30	4.8
S IV	744.904	0.00	0.249	47.30	—
S IV	748.393	0.00	0.459	47.30	—
S IV*	750.221	951.4	0.597	47.30	4.8
S IV*	753.760	951.4	0.131	47.30	4.8
S IV	809.656	0.00	0.118	47.30	—
S IV*	815.941	951.4	0.085	47.30	4.8
S V	786.468	0.00	1.360	72.68	—
S VI	933.378	0.00	0.436	88.05	—
S VI	944.523	0.00	0.215	88.05	—

Table 3
(Continued.)

Ion ⁽¹⁾	$\lambda^{(2)}$ (Å)	$E_{low}^{(3)}$ (cm ⁻¹)	$f^{(4)}$	IP ⁽⁵⁾ (eV)	$\log(n_{e,crit})^{(6)}$ log(cm ⁻³)
Ar IV	850.605	0.00	0.043	59.81	—
Ar V	705.353	0.00	0.061	75.04	—
Ar V	822.174	0.00	0.520	75.04	—
Ar VI	544.730	0.00	0.218	91.01	—
Ar VI	548.900	0.00	0.433	91.01	—
Ar VI	754.930	0.00	0.071	91.01	—
Ar VI*	767.065	2207.10	0.488	91.01	6.1
Ar VII	585.748	0.00	1.210	124.40	—
Ar VIII	700.240	0.00	0.375	143.45	—
Ar VIII	713.801	0.00	0.180	143.45	—
Ca IV	655.998	0.00	0.022	67.15	—
Ca V	637.917	0.00	0.014	84.43	—
Ca V	646.534	0.00	0.040	84.43	—
Ca V*	651.531	3275.6	0.053	84.43	6.3
Ca VI	629.602	0.00	0.016	108.78	—
Ca VI	633.844	0.00	0.032	108.78	—
Ca VI	641.904	0.00	0.049	108.78	—
Ca VII	624.385	0.00	0.058	127.70	—
Ca VII*	639.150	4071.4	0.066	127.70	7.5
Ca VIII	582.845	0.00	0.078	147.40	—
Ca VIII*	597.935	4308.3	0.063	147.40	6.9
Ca X	557.765	0.00	0.326	211.30	—
Ca X	574.010	0.00	0.160	211.30	—

Note. —

⁽¹⁾ Ions with one or more troughs detected in outflows observed in HST GO 14777.

⁽²⁾ Rest wavelength of observed transitions.

⁽³⁾ Lower-level energy of these transitions from the National Institute of Standards and Technology (NIST) database (Kramida et al. 2018), except for Ar VI* λ 767.06, which is from Verner, Verner & Ferland (1996).

⁽⁴⁾ Transition's oscillator strengths from the NIST database, except for Ar V, Ar VI, and Ca IV – Ca VIII, which are from Fischer et al. (2006) (see details in Paper V).

⁽⁵⁾ Ionization potential, which gives the energy required to ionize the element to the next stage of ionization (Allen 1977).

⁽⁶⁾ The logarithm of the critical electron number density for the excited transitions. The $n_{e,crit}$ values are from CHIANTI version 7.1.3 with assuming a temperature of 20,000 K (Landi et al. 2013).

⁽⁷⁾ The ionic transitions that are observed in SDSS J1042+1646 are shown in red.

⁽⁸⁾ We discuss the O V* multiplet in section 4.2.3.

spectrum is shown in figure 1. For the 2017 epoch, we marked the strong absorption lines related to these five outflow systems with colored dashed lines (system 1a and 1b are merged for simplicity, see section 4.1).

3.3. Synthetic Spectral Simulation

The main method to analyze AGN outflows involves the following steps: 1) identifying outflow systems at distinct velocities; 2) measuring ionic column densities (N_{ion}) of their absorption troughs using three standard methods, i.e., Apparent Optical Depth (AOD), Partial Covering (PC), and Power Law (PL); and 3) comparing these N_{ion} with the predictions from photoionization models to determine the physical properties for each outflow (e.g., Hamann et al. 2001; Arav et al. 2001, 2012, 2018; Borguet et al. 2012a, 2013; Chamberlain & Arav

2015; Xu et al. 2019a). The AOD method assumes that at every velocity the outflow completely and homogeneously covers the emission source (see, e.g., Savage & Sembach 1991). The PC method assumes a constant optical depth over a fraction of the emission source for every velocity (see, e.g., Edmonds et al. 2011). The PL method assumes the outflow at each velocity completely covers the emission source but has a varying optical depth across the source in the form of a power law (see, e.g., Arav et al. 2005).

For most of the previous works, the diagnostic absorption lines were within the $\lambda_{rest} > 1050$ Å. The above method works well in this range since there is a relatively small number of absorption troughs (mainly Ly α , C iv, N v, Si iv, and in rare cases P v, and S iv). Blending of these absorption troughs between different outflow systems is minimal to moderate in most of the cases.

This analysis method is inadequate for the EUV500 band since the EUV500 band includes outflow troughs from ~ 70 individual transitions. The atomic properties for these detected transitions are shown in table 3 and the ionic transitions observed in SDSS J1042+1646 are marked in red. With more troughs and multiple outflow systems, trough blending is more severe than in the $\lambda_{rest} > 1050$ Å range, especially when the absorption troughs are wide [e.g., see the panel 2 in figure 1 (Continued)]. Therefore, it is difficult to measure N_{ion} directly for most of the observed troughs in the EUV500. Similarly, it is impractical to measure upper limits for all possible transitions (~ 850 are within the wavelength range covered in these data alone).

For these reasons, we developed a Synthetic Spectral Simulation (SSS) method, which allows us to fit the multitude of troughs and determine the photoionization solutions more efficiently and accurately. While SSS may appear to be superficially similar to the spectral synthesis code SimBAL (Leighly et al. 2018), these two methods are philosophically quite different and to date have been applied to different rest-wavelength bands. The main analyzing steps of SSS are:

(1) Instead of directly measuring N_{ion} of each absorption trough, we only measure the uncontaminated absorption troughs. For doublet transitions which are not heavily saturated, we obtain N_{ion} measurements using the PC method as described in Arav et al. (2008). For saturated transitions, we use the AOD N_{ion} and treat them as lower limits. For singlet transitions with a maximum optical depth, τ_{max} , greater than 0.5, we treat the AOD N_{ion} as lower limits. For absorption troughs with $\tau_{max} < 0.05$, we determine the AOD N_{ion} as upper limits. For singlet transitions with $0.05 < \tau_{max} < 0.5$ and where the outflow shows other absorption troughs with $\tau > 2$ from ionic transitions with similar ionization, we treat the singlets' AOD N_{ion} as measurements since they are minimally affected by saturation effects ($< 10\%$).

(2) We then use these N_{ion} as a basis to determine a preliminary photoionization solution (PI₁). Photoionized plasma in an AGN outflow is characterized by the total hydrogen column density, N_H , and the ionization

parameter, U_H , where

$$U_H = \frac{Q_H}{4\pi R^2 n_H c} \quad (1)$$

Q_H is the source emission rate of hydrogen ionizing photons, R is the distance of the outflow from the central source, n_H is the hydrogen number density (for a highly ionized plasma, $n_H \simeq 0.8 n_e$), and c is the speed of light.

We run the spectral synthesis code Cloudy [version c17.00, Ferland et al. (2017)] to generate grids of photoionization simulations. We assume a spectral energy distribution (SED) and a metallicity (e.g., Arav et al. 2013, and see elaboration in section 4.1.2). We vary $\log(U_H)$ between -3.0 and 3.0, and $\log(N_H)$ between 17.0 to 24.0 [hereafter, $\log(N_{ion})$ is in units of $\log(\text{cm}^{-2})$] in steps of 0.05 dex. At each grid point, Cloudy predicts the N_{ion} for all ions in its database.

For each unblended absorption trough from a given ionic transition, we fit their optical depth profile in velocity space by a Gaussian profile as:

$$\tau(v) = \frac{A}{\sigma\sqrt{2\pi}} \times \exp\left(-\frac{(v - v_c)^2}{2\sigma^2}\right) \quad (2)$$

where $\tau(v)$ is the optical depth profile of the absorption trough, v is the velocity, A is the scaling factor, σ is the velocity dispersion and v_c is the velocity centroid of the Gaussian profile. $\frac{A}{\sigma\sqrt{2\pi}}$ is the maximum τ of the trough from the model. For each outflow system, we find the best v_c and σ by fitting the detected unblended absorption troughs.

For each ion, A in equation (2) is scaled according to the predicted value of N_{ion} based on PI₁ (e.g., Savage & Sembach 1991; Edmonds et al. 2011):

$$\begin{aligned} N_{ion} &= \int N(v) dv \\ &= \int \frac{3.8 \times 10^{14}}{f \cdot \lambda} \cdot \frac{A}{\sigma\sqrt{2\pi}} \times \exp\left(-\frac{(v - v_c)^2}{2\sigma^2}\right) dv \end{aligned} \quad (3)$$

where $N(v)$ is the velocity distribution of N_{ion} ($\text{cm}^{-2} \text{ km}^{-1} \text{ s}$), f is the oscillator strength of the corresponding ionic transition, and λ is the rest wavelength of the transition.

(3) We assume that all troughs in a given outflow system can be modeled using a Gaussian $\tau(v)$ function (see equation 2) with the same v_c and σ determined from the unblended absorption troughs of each outflow system. We vary A to match the N_{ion} predicted from PI₁, creating a full, AOD optical depth model for the entire observed spectrum. This model is then used to produce a synthetic spectrum which we overlay on top of the data. Since PI₁ has a minimal number of constraints (no constraints from blended troughs and maybe a few upper limits), there could be predicted troughs that conflict with the data. Therefore, we first look for predicted troughs that violate the τ_{max} upper limit threshold (discussed in step (1) above) within the continuum portion of the data so that we can measure additional upper limits. For example, PI₁ for S1a did not include the upper limit from O III. Inspection of the continuum region around the O III 833, O III* 834, and O III* 835 transi-

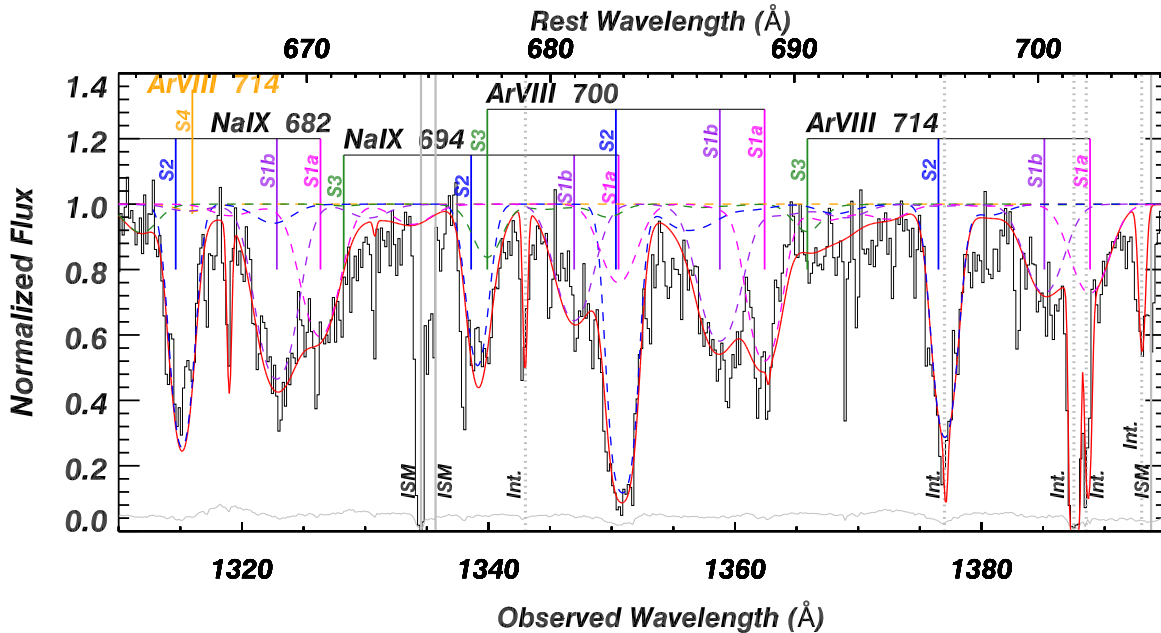


Figure 2. Best-fitting SSS models to the Ar VIII and Na IX region. The black and gray histograms show the normalized flux and the corresponding error for the 2017 epoch, respectively. We label the five outflow systems of the 2017 epoch and plot our models for them in magenta (S1a), purple (S1b), blue (S2), green (S3), and orange (S4) dashed curves (see section 3.2 for details). The solid red lines are the full SSS model by adding these five outflow systems. Strong Galactic ISM lines are shown in gray solid lines and marked with “ISM” at the bottom of the plot. Similarly, we mark the known intervening systems by “Int.” and plot them as the gray dotted lines.

tions marked in Figure 1 showed predicted troughs from PI_1 that were not supported by the data (τ_{max} exceeded 0.05 for the strongest transitions at those wavelengths). Additional models are then created using U_{H} and N_{H} values that are on the boundary of the 1σ contour for PI_1 and inspected to ensure that all upper limits are found.

(4) A new photoionization solution, PI_2 , is determined for each outflow including any newly measured upper limits, and another synthetic spectrum is created. As an example, for S1a this resulted in a decrease in N_{H} by 0.1 dex and an increase in U_{H} by 0.03 dex for the high ionization phase (compared to PI_1) and no change in the very-high ionization phase (see section 4.1.2). The blended troughs are then inspected for regions where none of the outflows have predicted troughs that can account for the observed absorption (none were found in these data). For such instances, the 1σ contour of PI_2 is probed for all outflows like what was done in step (3), and if only one outflow trough is found that can match the absorption, a new lower limit (or in rare cases involving doublets, a measurement) can be made.

(5) A final solution (PI) is then created from all measurements and limits. As a final check, the unblended troughs yielding the measurements that produced PI_1 are visually inspected to ensure that there are not any contaminating troughs that would make the measurements unreliable. As an example of the final results, we show the overall fit to the data (see figure 2), where we use the SSS solutions derived in section 4.1 – 4.3. The colored dashed lines are for different outflow systems, while the solid red lines are the overall model achieved by summing all outflow systems.

(6) To determine R , we use troughs from density sensitive transitions to obtain n_{e} (e.g., Hamann et al. 2001; Korista et al. 2008; Borguet et al. 2012a; Arav et al. 2013;

Xu et al. 2019a). We vary the n_{e} of the outflow systems to fit the troughs of transitions from excited states (see section 4.2.3 as an example).

Overall, the SSS is a three-dimensional model in the parameter space of U_{H} , N_{H} , and n_{e} . The detailed analysis for each outflow system is shown step by step in section 4, and we discuss the strengths and caveats of this method in section 6.

4. ANALYSIS OF EACH OUTFLOW SYSTEM

In the five outflow systems, we observed strong absorption troughs from 1) high-ionization species, such as N IV, O III, O IV, O V, and Ca VI, which have comparable ionization potential (IP) to the ionic transitions seen in HiBALs, e.g., C IV, Si IV and N V, from $\text{IP} \simeq 45 - 100$ eV. 2) very high-ionization species including Ar VIII, Ne VIII, Na IX, and Mg X, with $\text{IP} \simeq 100 - 500$ eV. 3) transitions from excited states, e.g., O IV*, O V*, and Si IV*, which are used to determine the n_{e} of the outflows. In our HST/COS spectra, we do not observe absorption troughs from any low-ionization species, which have IP smaller than O III ($\text{IP} = 54.93$ eV). Moreover, SDSS J1042+1646 was observed in 2006 by the Sloan Digital Sky Survey (SDSS) in 1930 – 4600 Å rest-frame. We found no absorption troughs from the low-ionization ion transitions of Mg II $\lambda\lambda 2796.35, 2803.53$ ($\text{IP} = 15.03$ eV). Therefore, none of the outflows make SDSS J1042+1646 a low-ionization BALQSO (Voit et al. 1993).

The absorption troughs from outflow S1, S2, and S3 are consistent with no trough variability between the 2011 and 2017 epochs. However, S4 shows a velocity shift of -1550 km s^{-1} between the two epochs. The remarkable behavior of S4 is described in Paper IV. In this paper, we take into account the blending of troughs from S4, which helps the analysis of the other three outflow systems.

Table 4
Column Densities for Outflow Systems in SDSS J1042+1646

Ion	$\lambda^{(1)}$ (Å)	$N_{ion,mea}^{(2)}$ $\log(\text{cm}^{-2})$	$\frac{N_{ion,mea}^{(3)}}{N_{ion,model}}$ 1
Outflow System 1a, $v = [-5300, -4500]^{(4)}$			
H I	972.54	>15.32	>0.09
O III	702.34	<14.80	<0.77
O IV	787.71	>15.19	>0.05
O V	629.73	>15.24	>0.01
Ne VIII	770.41, 780.32	>16.40	>0.06
Na IX	682.72, 694.15	$15.59^{+0.15}_{-0.10}$	1.00
Mg X	609.79, 624.94	>16.04	>0.21
S IV	657.32	$14.19^{+0.10}_{-0.13}$	1.11
S V	786.47	>14.04	>0.42
Ar V	822.17	<15.21	<5
Ar VII	585.75	>14.48	>0.53
Ar VIII	700.24, 713.80	$15.09^{+0.13}_{-0.12}$	0.91
Ca VI	633.84	$14.69^{+0.12}_{-0.10}$	1.00
Ca VIII	582.85	>15.43	>0.50
Outflow System 1b, $v = [-6400, -5300]^{(4)}$			
H I	1025.72	>15.29	>0.09
N III	685.52	<14.47	<1.43
O III	832.93	<14.81	<0.77
O IV	787.71	>15.59	>0.12
O V	629.73	>15.43	>0.02
Ne VIII	770.41, 780.32	>16.38	>0.04
Na IX	682.72, 694.15	$15.85^{+0.15}_{-0.16}$	1.11
Mg X	609.79, 624.94	>16.16	>0.15
S IV	657.32	$13.93^{+0.15}_{-0.14}$	0.91
S V	786.47	>14.76	>2.00
Ar V	822.17	<15.18	<5.00
Ar VII	585.75	>14.73	>0.83
Ar VIII	700.24, 713.80	$15.09^{+0.12}_{-0.15}$	0.83
Ca VI	633.84	$14.77^{+0.12}_{-0.11}$	1.11
Outflow System 2, $v = [-8100, -6900]^{(4)}$			
H I	1025.72	>15.88	>0.33
N IV	765.15	>15.34	>0.91
O III	702.34	<14.67	<2.5
O IV	608.40	>16.25	>1.0
Ne VIII	770.41, 780.32	>16.43	>0.06
Na IX	682.72, 694.15	$15.55^{+0.16}_{-0.12}$	0.95
Mg X	609.79, 624.94	>16.57	>0.77
S IV	657.32	<13.38	<1.11
Ar V	822.17	<15.60	<10.0
Ar VIII	700.24, 713.80	$15.30^{+0.12}_{-0.10}$	1.00
Ca VI	641.90	$14.90^{+0.12}_{-0.15}$	1.11

Here, we report the detailed analyses of S1, S2, and S3. The N_{ion} for the 2017 epoch are presented in table 4. For each system, the measured column densities ($N_{ion,mea}$) summed over all observed energy states are reported in the third column. The ratios of measured to the modeled column densities (i.e., $N_{ion,mea}/N_{ion,model}$) from the SSS method are reported in the fourth column. When we have $N_{ion,mea}$ as a lower limit, we expect $N_{ion,model} > N_{ion,mea}$, therefore, $N_{ion,mea}/N_{ion,model} < 1$ and vice versa.

4.1. Outflow System 1 ($v = -5300 \text{ km s}^{-1}$)

4.1.1. Kinematics and N_{ion} Determinations

S1 has strong absorption troughs from both high-ionization species, such as O III, O IV, and Ca VI, and very high-ionization species, including Na IX, Mg X, and Ne VIII. In figure 3, we show the kinematics of the absorption troughs for both the 2011 and 2017 epochs in green and purple, respectively. The troughs from

Table 4
(Continued.)

Ion	$\lambda^{(1)}$ (Å)	$N_{ion,mea}^{(2)}$ $\log(\text{cm}^{-2})$	$\frac{N_{ion,mea}^{(3)}}{N_{ion,model}}$ 1
Outflow System 3, $v = [-10500, -9500]^{(4)}$			
H I	1025.72	>15.61	>0.30
N IV	765.15	>14.84	>0.26
O IV	608.40	$16.27^{+0.12}_{-0.10}$	1.00
Ne VIII	770.41, 780.32	>15.92	>0.15
Na IX	682.72, 694.15	<15.68	<10.0
Mg X	609.79, 624.94	$15.51^{+0.15}_{-0.14}$	1.00
Ar V	822.17	<14.99	<3.33
Ar VI	754.93	>14.72	>1.11
Ar VIII	700.24, 713.80	<14.61	<0.83
Ca VI	641.90	<14.95	<1.43
Ca VII	624.39	$15.30^{+0.16}_{-0.13}$	1.11

Note. —

(1) Rest wavelengths of the measured transitions. For doublet or multiplet transitions, we show all the uncontaminated/measurable rest wavelengths.

(2) Measured N_{ion} by PC or AOD method (see section 3.2). Lower limits are shown in blue, while upper limits are shown in red.

(3) Ratio of the measured N_{ion} to the model predicted N_{ion} (see section 4) .

(4) N_{ion} integration range in km s^{-1} .

–7000 km s^{-1} to –4000 km s^{-1} show double-minima features, which are most apparent in the Na IX-b, Ar VII and Ar VIII-b [hereafter, the “-b” or “-r” suffix stands for the shorter (bluer) or longer (redder) wavelength component of doublet transitions, respectively]. Since these two features appear at the same velocity in several troughs, we divide S1 into two components, 1a and 1b, which are centered at –4950 km s^{-1} and –5750 km s^{-1} , respectively. For each individual ion, we report the measured N_{ion} for the 2017 epoch in table 4.

The N_{ion} measurements used for the initial U_H and N_H solution are from the Na IX and Ar VIII doublet transitions, and they are determined in the following ways: 1) For the Na IX doublets in component 1b, we assume each trough is symmetric since the troughs are well fitted with Gaussian profiles (see figures 2 & 3) and solve for N_{ion} by using the PC equations on the unblended high-velocity wing. We then double the value to obtain the measurement. 2) Similarly, for the Ar VIII doublet in components 1a and 1b, the Ar VIII-r is contaminated by 2 intervening systems. Therefore, the unblended half of the troughs are used to solve the PC equations. Then, we double the values for the N_{ion} measurements. 3) The Na IX-r in component 1a is blended with the Ar VIII-b trough from S2. If no other information is available, we treat AOD N_{ion} value derived from the Na IX-b as a lower limit. However, the Ar VIII doublet of component 1a is not saturated and is deeper than the Na IX-b absorption, while Ar VIII and Na IX have similar IPs. Therefore, we can safely treat the AOD N_{ion} value derived from the Na IX-b as a measurement.

Given the signal-to-noise (S/N) of the data and differ-

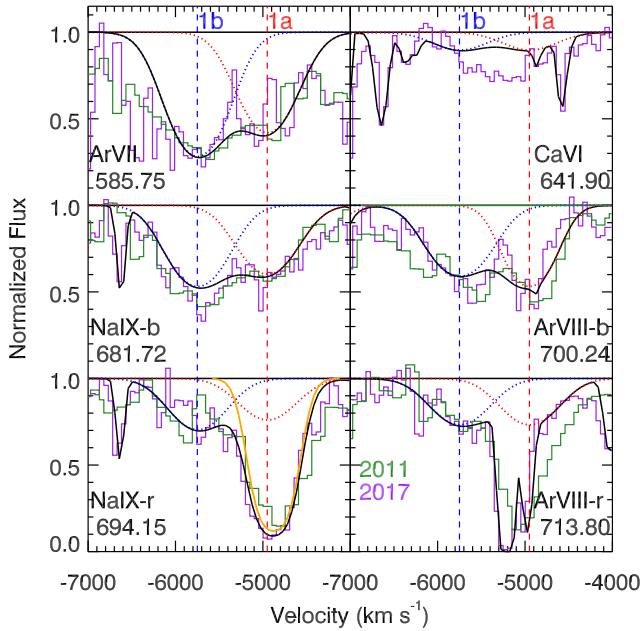


Figure 3. Comparison between the data and SSS models for the absorption troughs in components 1a and 1b of S1, where their velocity centers are marked by the red and blue dashed lines at -4950 km s^{-1} and -5750 km s^{-1} , respectively. The normalized spectrum is shown in green for the 2011 epoch and purple for the 2017 one. The best-fitting SSS models for components 1a and 1b are shown as red and blue dotted lines while the combined full model for each region is shown as the black solid lines. We mark the blue or red component of a doublet by adding a letter “b” or “r” after its ion label. In the Na IX-r panel, the absorption from Ar VIII-b of outflow S2 is shown as the orange solid line. Strong intervening systems are modelled by narrow Gaussian profiles and are added to the full model, i.e., at $v \sim -6600 \text{ km s}^{-1}$ in the Na IX-b and Na IX-r region; $v \sim -4950$ and -5200 km s^{-1} in the Ar VIII-r region; $v \sim -4600$, -6350 , and -6600 km s^{-1} in the Ca VI region.

ent spectral resolution of the observations, the absorption troughs are consistent with no variation between the two epochs for most of the ions. An exception is the low-velocity wing of the Ar VIII-r absorption trough. However, the entire Ar VIII-b troughs are consistent with no variations between the 2011 and 2017 epochs. Therefore, the deviation in Ar VIII-r is not intrinsic to the outflow system and may be due to calibration issues.

Ca VI has three transitions at 629.60 \AA , 633.84 \AA , and 641.90 \AA , where their f ratios are almost 1:2:3, respectively. Ca VI $\lambda 629.60$ and $\lambda 633.84$ are not measurable, since the former coincides with the strong O V $\lambda 629.73$ and the latter is blended with two intervening systems. However, we observed shallow absorption troughs from Ca VI $\lambda 641.90$, i.e., $\tau_{\text{max}} < 0.2$. Therefore, the AOD N_{ion} derived will be close to the actual N_{ion} value (see elaborations in section 2.9 Leighly et al. (2011) and 5.4 of Arav et al. (2013)). Thus, we treat the AOD N_{ion} from the absorption trough of Ca VI $\lambda 641.90$ as a measurement. Similarly, for S IV $\lambda 657.32$, we are able to measure the AOD N_{ion} of it for both component 1a and 1b. We treat them as N_{ion} measurements since they have $\tau_{\text{max}} < 0.3$.

The strongest two observable transitions from O III are at 702.34 \AA and 832.93 \AA , and both are consistent with no absorption. We get an upper limit on N_{ion} for O III from the AOD measurement of the stronger f transition at 702.34 \AA . Since oxygen is the most abundant metal, the non-detection of O III hints that none of the doubly

ionized species would be strong enough to be detected in our spectrum. Indeed, the troughs from N III are consistent with no absorption.

The other ionic transitions are either saturated or undetected. Therefore, the AOD N_{ion} for these two types are treated as lower and upper limits, respectively.

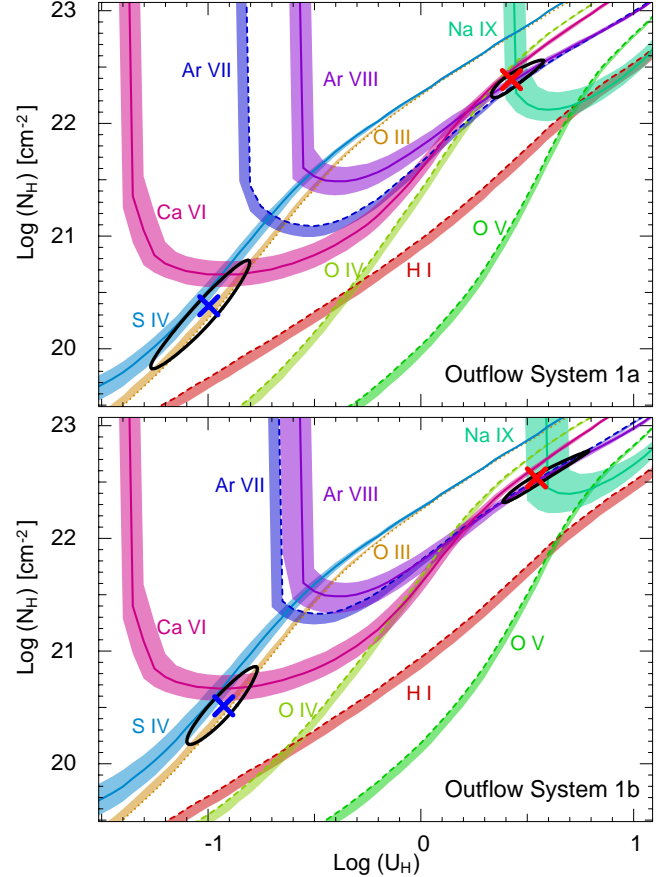


Figure 4. The best-fitting photoionization solution for components 1a and 1b of S1 in epoch 2017. Each colored contour represents the region where the $(N_{\text{H}}, U_{\text{H}})$ model predicts consistent N_{ion} with the observed ones. Solid lines represent N_{ion} measurements, while dashed lines and dotted lines represent lower and upper limits, respectively. The very high- and high-ionization phase solutions are shown by the red and blue “x” along with their 1σ error contours in the black ellipses, respectively. All other N_{ion} in table 4 that are not shown here are lower or upper limits which are consistent with the solutions and are omitted for clarity’s sake.

4.1.2. SSS Models and Photoionization Solutions

After we determined N_{ion} for unblended troughs, we follow the SSS method in section 3.3 to get the best-fitting photoionization model for all observed troughs. To account for systematics in the unabsorbed emission model, the adopted N_{ion} lower limits assume lower errors of 20%, and N_{ion} upper limits assume upper errors of 20%. We assume solar metallicity (Grevesse et al. 2010) and the HE0238 SED (Arav et al. 2013). This SED is based on observations of quasar HE0238–1904 in a similar rest-frame wavelength range to our object (Arav et al. 2013). For the observed data ($570\text{--}1000 \text{ \AA}$ rest-frame), the ratio of the HE0238 SED with the SDSS J1042+1646 continuum is constant to within $\pm 10\%$. The

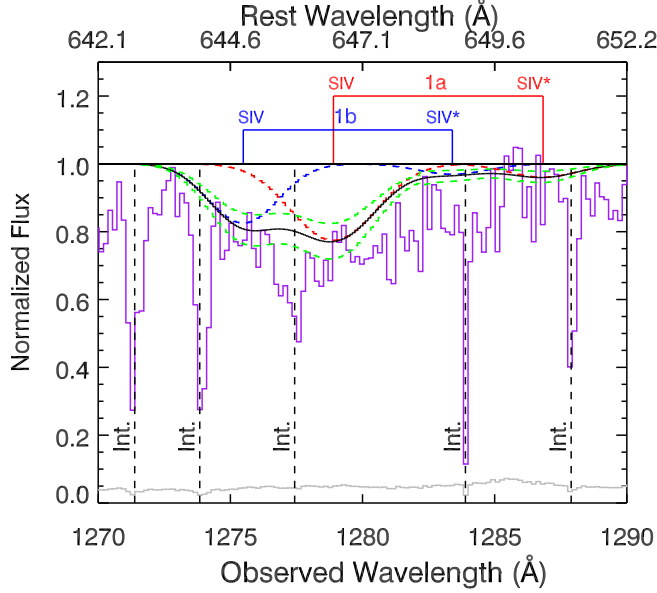


Figure 5. SIV $\lambda 657.32$ and SIV* $\lambda 661.40$ regions for components 1a and 1b from S1. The purple and gray solid histograms are the normalized flux and errors for the 2017 epoch, respectively. The red and blue lines are for component 1a and component 1b, respectively. Based on our best-fitting photoionization solution, we show the predicted absorption troughs of SIV $\lambda 657.32$ and SIV* $\lambda 661.40$ in red and blue dashed lines. The full absorption model is shown as the solid black line, while strong intervening systems are marked with black dashed lines. We increase and decrease the optical depth such that the change in flux at the centers of the Gaussian profiles equal the noise level at that wavelength and adopt them as the lower and upper bounds in fitting the troughs, respectively. These bounds are shown in green dashed lines.

best-fitting model is shown as the black solid lines in figure 3. Absorption troughs from components 1a and 1b are plotted separately as blue and red dotted lines. The ratios of measured N_{ion} to the model predicted N_{ion} are presented in the 4th column in table 4.

Arav et al. (2013) demonstrated that detections of both the very high-ionization troughs (e.g., Ne VIII and Mg X) and high-ionization troughs (e.g., O IV) in the same outflow state two ionization phases for the absorber. We find the same situation in all of the outflow systems discussed here. Figure 4 shows the models' corresponding photoionization solution. For component 1a (see top panel of figure 4), the very high-ionization phase (VHP) is marked as the red cross and is mainly constrained by the N_{ion} measurements of Na IX and Ar VIII. However, this VHP underestimates the observed $N(\text{SIV})$ by over a factor of 1000. Moreover, if we shift this VHP vertically up to match the $N(\text{SIV})$ curve at $\log(N_H) = 22.78$, the solution will overpredict the $N(\text{Ar VIII})$ by a factor of 13 and $N(\text{Ca VI})$ by a factor of 22. Therefore, a pure VHP solution is unable to produce all of the observed N_{ion} . The high-ionization phase (HP) is marked by the blue cross and produces the observed $N(\text{SIV})$ and is constrained by the N_{ion} upper limit of O III. However, this HP produces negligible amounts of the observed $N(\text{Ar VIII})$ and $N(\text{Na IX})$. Therefore, we invoke a two-phase ionization solution. The very high-ionization phase (VHP) has $\log(N_H) = 22.37^{+0.19}_{-0.12}$, and $\log(U_H) = 0.42^{+0.16}_{-0.09}$, and the high-ionization phase (HP) has $\log(N_H) = 20.39^{+0.40}_{-0.58}$ and $\log(U_H) = -0.98^{+0.17}_{-0.30}$. The N_{ion} upper limits from N III,

S V, and Ar V, and the lower limits from Ne VIII, Mg X, and Ca VIII are consistent with this two phase solution and omitted for clarity's sake.

Similarly, component 1b (see the bottom panel of figure 4), has a VHP at $\log(N_H) = 22.51^{+0.27}_{-0.21}$ and $\log(U_H) = 0.54^{+0.24}_{-0.16}$, and a HP at $\log(N_H) = 20.52^{+0.36}_{-0.34}$ and $\log(U_H) = -0.93^{+0.17}_{-0.18}$. We discuss and compare the two-ionization phase solutions to former studies in section 6.1.

4.1.3. Determinations of n_e From SIV and SIV*

The most robust way for determining the distance, R , from the ionizing source of an absorption outflow is to use the troughs from ionic excited states. The ratio between the N_{ion} from excited and ground states, e.g., $N(\text{SIV}^*)/N(\text{SIV})$, yields n_e for an outflow, and combined with the value of U_H , R can be determined (See equation (1). e.g., Borguet et al. 2013; Chamberlain et al. 2015; Arav et al. 2018; Xu et al. 2018, 2019a).

For component 1a, we observed the absorption troughs from the strongest SIV transition at 657.32 \AA and the corresponding excited state at 661.40 \AA both with oscillator strengths, $f \sim 1.18$. For the 2017 data, we show our best-fitting SSS model for the SIV region in figure 5. We clearly have a deeper feature in the SIV $\lambda 657.32$ region than in the SIV* $\lambda 661.40$ region for component 1a. This yields $\log[N(\text{SIV})] = 14.19^{+0.10}_{-0.13}$ and $\log[N(\text{SIV}^*)] = 13.35^{+0.11}_{-0.12}$. Following the same method described in section 2 of Xu et al. (2019a), we derive $\log(n_e) = 3.68^{+0.18}_{-0.25}$ for component 1a [hereafter, $\log(n_e)$ is in units of $\log(\text{cm}^{-3})$].

Similarly, for component 1b, the absorption trough from SIV $\lambda 657.32$ shows a deeper feature than SIV* $\lambda 661.40$, while the latter cannot be much deeper than the current modeling due to the flux level on the two shoulders (see figure 5). We get $\log[N(\text{SIV})] = 13.93^{+0.14}_{-0.13}$ and $\log[N(\text{SIV}^*)] = 13.21^{+0.10}_{-0.13}$. This leads to $\log(n_e) = 3.78^{+0.23}_{-0.26}$, which is consistent with the n_e result for component 1a within the errors. This strengthens the possibility that both outflows originate from the same absorber. After we determine n_e for the outflows, R can be derived (see section 5).

4.2. Outflow System 2 ($v = -7500 \text{ km s}^{-1}$)

S2 also shows absorption troughs from both high- and very high-ionization species. Moreover, S2 has deep absorption troughs near its expected O v* multiplet region. We begin by determining the N_{ion} and constructing the photoionization solutions. Following that, we model the O v* regions and derive the constraints for n_e and R .

4.2.1. Kinematics and N_{ion} Determinations

We show the strong absorption troughs for S2 in figure 6, where the 2011 and 2017 epochs are shown in green and purple colors, respectively. The data is consistent with no variability between the 2011 and 2017 epochs. We report the measured N_{ion} in table 4 and discuss them in detail here.

Similar to S1, we adopt the PC method and get N_{ion} measurements from the unblended and well-separated Na IX and Ar VIII doublets. The Ne VIII and Mg X doublet troughs are black at their deepest points, so

their AOD N_{ion} from the red component are taken as lower limits. For the Ca VI triplet, the absorption trough from Ca VI at 629.60 Å and 633.84 Å are blended with the Galactic Ly α region, while the Ca VI λ 641.90 shows similar but shallower trough features as the Na IX doublet. After modeling out the contamination of intervening systems (i.e., at $v = -7050, -7320, -7720$ km s $^{-1}$) by narrow Gaussian profiles, the AOD N_{ion} value from the Ca VI λ 641.90 is treated as a measurement. The absorption troughs from other ion transitions are either lower or upper limits and are reported in table 4. The lack of detection from O III and lower IP ions demonstrates that this is not a low-ionization BALQSO.

4.2.2. SSS Models and Photoionization Solutions

We present the best-fitting SSS model as the black solid line in figure 6 for each trough and the corresponding photoionization solution in figure 7. Similar to S1, all of the observed troughs are well fitted by a two-phase photoionization solution. The VHP is constrained mainly by the N_{ion} measurements from Na IX and Ar VIII, and is supported by the N_{ion} from Ca VI. This yields $\log(N_H) = 22.40^{+0.12}_{-0.10}$ and $\log(U_H) = 0.4^{+0.12}_{-0.06}$. The HP is constrained by the upper limit from S IV, measurement of Ca VI, and the lower limits from O IV and N IV. This yields $\log(N_H) = 20.79^{+0.32}_{-0.34}$, and $\log(U_H) = -0.60^{+0.17}_{-0.14}$. Other ions from S2 that are not shown in figure 7 are consistent with the solutions.

4.2.3. Determination of n_e From the O v* Multiplet

The O v* transitions near 760 Å are the isoelectronic sequence of the C III* transitions near 1175 Å, which are sensitive to a wide range of n_e (Gabel et al. 2005; Borguet et al. 2012b; Arav, et al. 2015; Leighly et al. 2018). Our HST program shows the first clear detection of O v* absorption troughs in an AGN outflow, in both quasar SDSS J1042+1646 and PKS 0352-0711 (Paper V). For the O v* multiplet, there are six ($J - J'$) components of the $2s2p^3P_J - 2p^2^3P_{J'}$ multiplet between 758.7 Å and 762.0 Å (Doyle et al. 1983; Keenan et al. 1994). However, they are very rare to be observed in either emission or absorption. Previously, the only extra-terrestrial detections of O v* were in solar spectra. The O v* multiplet has been resolved as emission lines by the Harvard S-055 EUV spectrometer onboard Skylab (Doyle et al. 1983; Keenan et al. 1994) and more recently by the Solar Ultraviolet Measurements of Emitted Radiation (SUMER) on board the Solar and Heliospheric Observatory (SOHO) (O'Shea et al. 2000).

In the upper panel of figure 8, the ratio of each J level's population to that of the ground state is plotted as a function of n_e . In the bottom panel, we show the population ratios between different J levels versus n_e . When $\log(n_e) < 5$, the level population of O v* $_{J=0}$, i.e., $n(O v^*_{J=0})$, dominates, and $n(O v^*_{J=1})$ and $n(O v^*_{J=2})$ keep increasing as n_e grows in this region. In the $\log(n_e)$ range between 5 and 9, $n(O v^*_{J=2}) > n(O v^*_{J=0}) > n(O v^*_{J=1})$. $n(O v^*_{J=0})$ is populated quickly for high n_e , and finally reaches equilibrium at $\log(n_e) > 12$, where $n(O v^*_{J=2}) > n(O v^*_{J=1}) > n(O v^*_{J=0})$.

We observed significant absorption troughs at the expected locations of the O v* transitions. The best-fitting

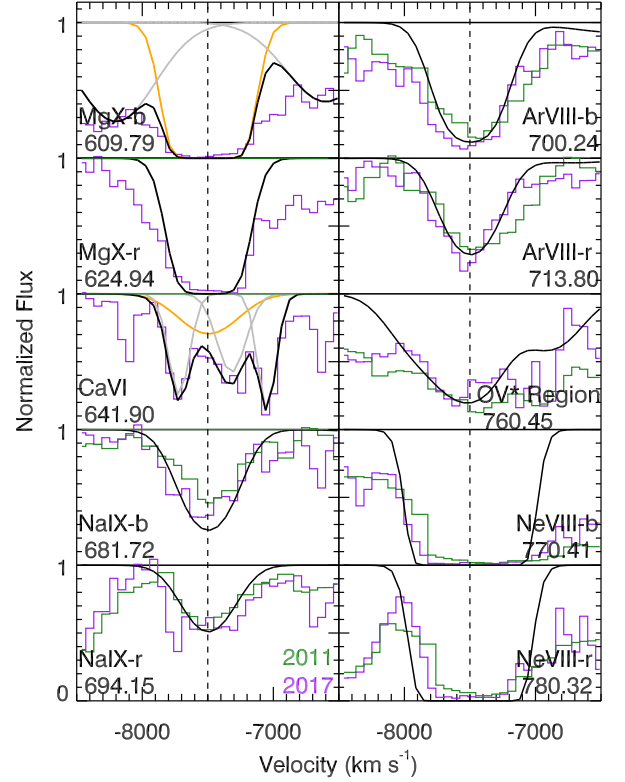


Figure 6. Comparison of data and SSS models for absorption troughs in S2. The velocity center for this system is marked as the black dashed line at -7500 km s $^{-1}$. The normalized spectrum is shown in green for the 2011 epoch and purple for the 2017 one. The best-fitting model for S2 is shown in black solid lines. For the Ne VIII and Mg X doublets, both the data and model are consistent with significant saturation. For Ca VI λ 641.90, we show the model for Ca VI and the intervening systems as the orange solid and gray dotted lines, respectively. For Mg X λ 609.79, we show the model for Mg X as an orange solid line, where contaminating troughs of O IV λ 608.40 from S1b (the Gaussian centered at $v = -6600$ km s $^{-1}$) and S2 (the Gaussian centered at $v = -8200$ km s $^{-1}$) are shown as gray dotted lines. See section 4.2.1 for details.

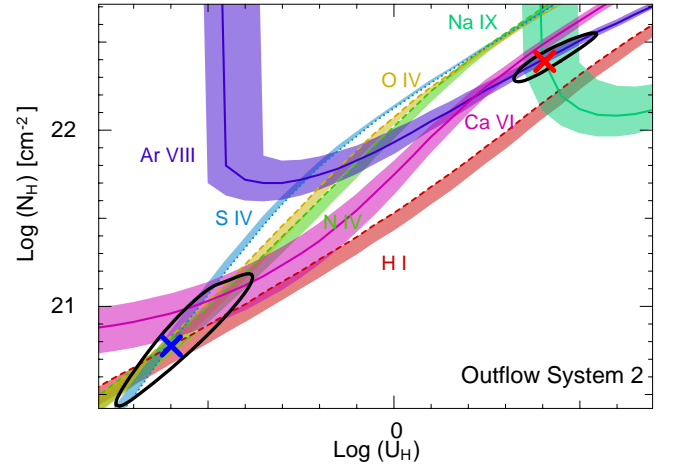


Figure 7. The best-fitting photoionization solution for S2. All patterns and labels are the same as in figure 4. All other N_{ion} in table 4 that are not shown here are lower or upper limits which are consistent with the solutions and are omitted for clarity's sake.

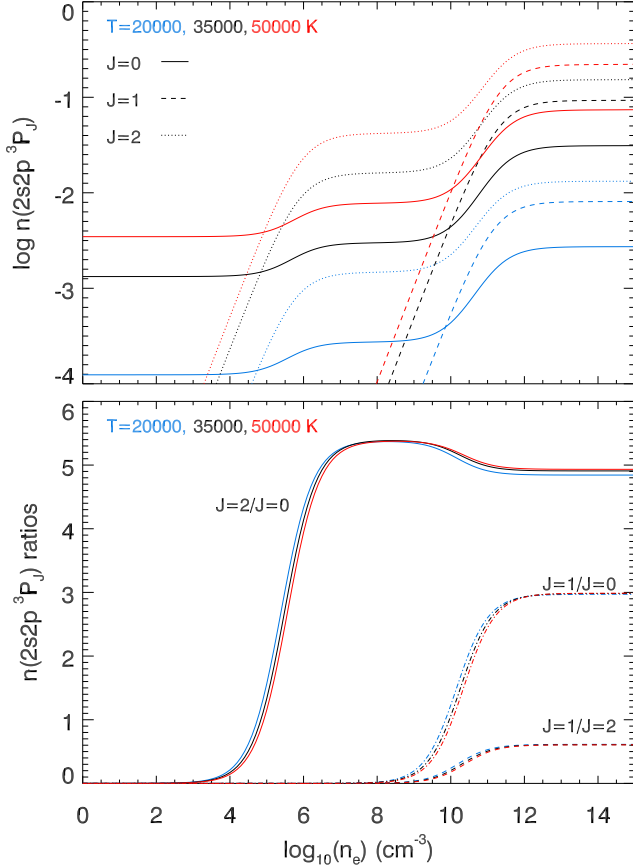


Figure 8. $O v^*$ level populations. **Top:** The computed populations for the 3P_J levels of the $2s2p$ term of O^{+4} are plotted as a function of electron number density [CHIANTI version 7.1.3 (Landi et al. 2013)]. We show the $J = 0, 1, 2$ levels in solid, dashed, and dotted lines, respectively. We show the temperature dependence of $n(O v^*)/n(O v)$ by presenting three different temperature curves. **Bottom:** Population ratios between different J levels of $O v^*$. See detailed discussions in section 4.2.3.

photoionization solution from SSS model predicts that the total $\log[N(O v)] = 17.02 \text{ cm}^{-2}$, with the ratio of contributions from the HP and VHP as $\sim 1:2$. The Cloudy predicted temperature for the HP and VHP are around $T_{low} = 21,000 \text{ K}$ and $T_{high} = 44,000 \text{ K}$, respectively. Due to the strong temperature dependence of $n(O v^*)/n(O v)$, the VHP produces 20 times more $N(O v^*)/N(O v)$ compared to the HP. Overall, most ($\sim 97.5\%$) of the $O v^*$ observed in the spectrum is from the VHP.

In order to fit the observed $O v^*$ region, we adopt the model predicted value for $N(O v)$ and temperature T_{high} . We vary $\log(n_e)$ from 5 to 13, in steps of 0.1 dex and show some of the fits to this range in figure 9. The black and gray histograms are the normalized flux and error for the 2017 epoch, respectively. The red dashed lines are the models for the $O v^*$ multiplet with the corresponding J values. The vertical line below each J value indicates the relative f of the line. We note that there are several “contaminations” from intervening systems at 1466.5 \AA , 1469.0 \AA and 1470.0 \AA .

Despite all of the intervening systems, we can still estimate n_e as shown in figure 9. The lower limit is determined at $\log(n_e) = 5.5$, where the model clearly underestimates the data by more than 1σ (see panel 1 and 2). The upper limit is determined to be $\log(n_e) = 6.3$, where

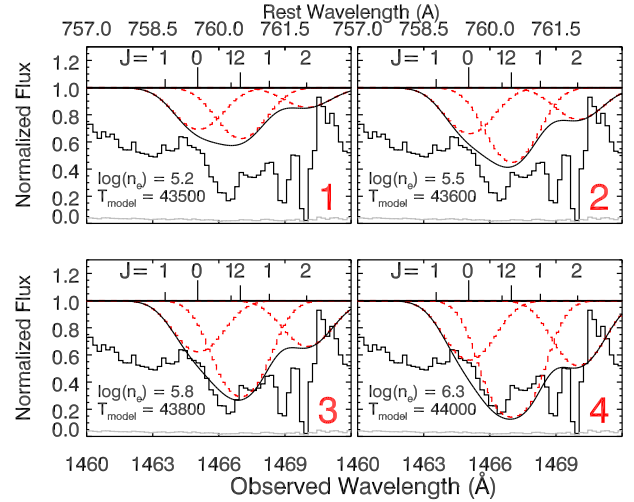


Figure 9. Fits to the $O v^*$ multiplet region for S2, where we vary n_e to get the best fit. The n_e of S2 and the corresponding temperature from Cloudy are shown at the bottom-left corner of each panel. The black and gray solid histograms are the normalized flux and errors for the 2017 epoch. For each subplot, the red dashed lines represent the models of the $O v^*$ multiplet for a particular n_e , while the black solid lines are the summation of all models in this region. The sharp features at $\sim 1466.5 \text{ \AA}$, 1469.0 \AA and 1470.0 \AA are intervening systems. We label the four panels as 1 – 4 at the bottom-right corner. See section 4.2.3 for a detailed discussion.

the model overestimates the data (see panel 4). We get the best fit when $\log(n_e) = 5.8$. Therefore, $\log(n_e) = 5.8^{+0.5}_{-0.3}$.

Besides $O v^*$, we observed troughs from other density sensitive transitions. However, they are either situated in a saturated region (Ne $v^* \lambda 572.33$ and $O iv^* \lambda 790.20$), or too weak to form a significant trough (S $iv^* \lambda 661.40$ and the corresponding S iv at 657.32 \AA). From the best-fitting photoionization solution model with the above-determined n_e , we are able to predict absorption troughs that are consistent with the data in the expected regions of these transitions.

4.3. Outflow System 3 ($v = -9940 \text{ km s}^{-1}$)

S3 also shows absorption troughs from both high- and very high-ionization species. We show the data and the best-fitting SSS models in figure 10. For the $O iv + Mg x$ -b region, the blue dotted lines are for the $O iv \lambda 608.340$ and $O iv^* \lambda 609.83$ troughs while the red dotted line is for the $Mg x \lambda 609.79$ trough. For the $Ca vii + Mg x$ -r region, the cyan and red dotted lines are for the $Ca vii \lambda 624.28$ and $Mg x \lambda 624.94$ troughs, respectively. These two regions fall in the gap of the HST/COS G140L grating in the 2011 epoch. For the $Ar viii$ -r and $Ar vi$ region, their modeled troughs are shown as orange dotted lines. The $Ar viii$ -r trough is consistent with the shallow observed absorption and is contaminated by the $Ar viii \lambda 700.24$ trough from S1a (centered at $-10,600 \text{ km s}^{-1}$ in the top-right panel of figure 10). Therefore, the AOD N_{ion} from the $Ar viii$ -r trough is treated as an upper limit. The higher velocity wing of the $Ar vi \lambda 754.93$ trough is contaminated by the $Ne viii \lambda 780.32$ trough from S4, while S4 shows variability between the 2011 and 2017 epochs. We discuss this variability in Paper IV.

We report the measured N_{ion} in table 4 and the best-fitting photoionization solution from the SSS model in

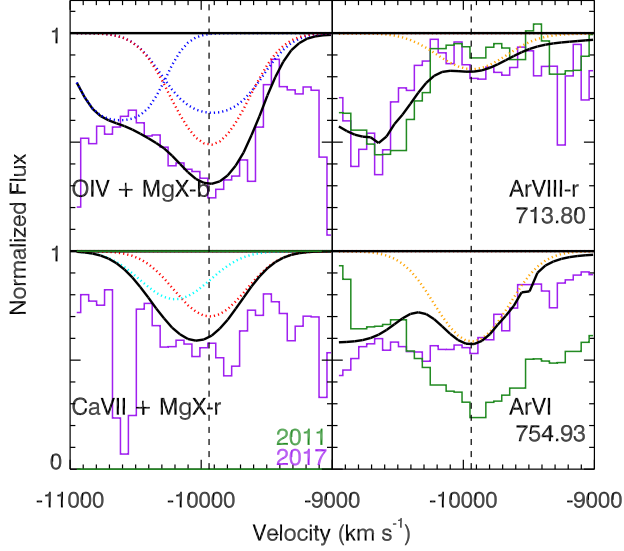


Figure 10. Comparison of the data with the SSS models for the absorption troughs in S3. The velocity center for this system is the black dashed line at -9940 km s^{-1} . The normalized spectrum is shown in green for the 2011 epoch and purple for the 2017 one. The best-fitting SSS models combining all outflow systems are shown as black solid lines. See section 4.3 for details.

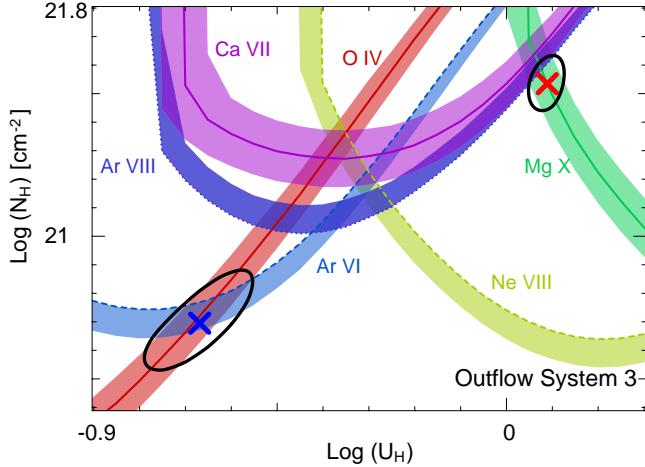


Figure 11. The best-fitting photoionization solution for S3. All patterns and labels are the same as figure 4.

figure 11. All observed outflow absorption troughs are well fitted by a two-phase ionization model. The observed amount $N(\text{Ca VII})$ originates from both the HP and VHP, with a ratio of $\sim 1:3$, respectively. Therefore, Ca VII gives constraints to both phases. The HP yields $\log(N_{\text{H}}) = 20.69^{+0.34}_{-0.28}$ and $\log(U_{\text{H}}) = -0.67^{+0.21}_{-0.31}$. This solution is constrained by the O IV and Ar VI troughs, as well as the Ca VII trough. The VHP gives $\log(N_{\text{H}}) = 21.54^{+0.17}_{-0.18}$ and $\log(U_{\text{H}}) = 0.09^{+0.08}_{-0.07}$. This solution is constrained mainly by the measured N_{ion} of the Mg X doublet and Ca VII, and the upper limit of Ar VIII. Comparing between the 2011 and 2017 epochs, the troughs of S3 show no variations.

We do not observe measurable absorption troughs from density diagnostic transitions for S3. Therefore, the n_{e} of S3 is undetermined.

5. DISTANCES AND ENERGETICS

Using the n_{e} determination for each outflow system, we can solve equation (1) for R . We then determine the mass flow rate (\dot{M}) and the kinetic luminosity (\dot{E}_{k}) by assuming the outflow is in the form of a thin and partially filled shell (see elaboration in Borguet et al. 2012a):

$$\dot{M} \simeq 4\pi\Omega RN_{\text{H}}\mu m_{\text{p}}v \quad (4)$$

$$\dot{E}_{\text{k}} \simeq \frac{1}{2}\dot{M}v^2 \quad (5)$$

where Ω is the global covering factor, i.e., the portion of the full solid angle covered by the outflow (for SDSS J1042+1646, we use $\Omega = 0.2$, see discussion in section 6.3), $\mu = 1.4$ is the mean atomic mass per proton, m_{p} is the proton mass, and v is the velocity of the outflow.

Since the Mg II emission region for SDSS J1042+1646 is observed by SDSS, we follow the Mg II-based black-hole mass estimators (calibrated with $\text{H}\beta$ reverberation measurement, see equation (7) and table (4) in Bahk et al. 2019) to derive a black hole mass of $10^{9.3}$ and corresponding Eddington luminosity, $L_{\text{Edd}} = 10^{47.4} \text{ erg s}^{-1}$. We then calculate the ratio of the outflow's kinetic luminosity to the L_{Edd} , i.e., $\Gamma_{\text{Edd}} \equiv \dot{E}_{\text{k}}/L_{\text{Edd}}$.

In table 5, we show all the physical parameters for the outflows we extracted from the data. In the first part of the table 5, we show the derived photoionization solutions, n_{e} , f_{v} (volume filling factor, see section 6.1.2), and the energetics for the four outflows analyzed in section 4. We show the “shading effect” results in the second part of the table (see section 6.2). Finally, we compare our derived physical parameters to two other energetic outflows in the third part of the table (see discussion in section 6.3).

6. DISCUSSION

6.1. The Two-phase Outflows

6.1.1. Prevalence of Outflows with a VHP

Two ionization phase outflows have been reported and discussed in detail for quasar HE0238–1904 (see section 8 in Arav et al. 2013). Their lower ionization phase (similar to HP in this paper) was mainly constrained by the N_{ion} from H I and O IV, while the higher-ionization phase (similar to VHP in this paper) was constrained by the N_{ion} from O VI, Mg X, and Ne VIII. Similarly, all of the outflows analyzed here (S1a, S1b, S2, and S3) as well as the 8 EUV500 outflows reported in three additional quasars (see Paper I), necessitate an HP and a VHP. All of these outflows show O IV troughs and therefore should have C IV 1549 Å troughs. Thus, these outflows would be classified as HiBALs if observed in rest-frame wavelengths, $\lambda_{\text{rest}} > 1050 \text{ Å}$ (see section 4.5 in Paper I). The existence of a VHP in all outflows from these quasars suggests that all HiBALs have VHPs, which is not practically accessible with ground-based telescopes (see section 1). The selection criteria of the EUV500 sample do not affect the extrapolation of these results to the general HiBAL outflow population (see section 4.1 in Paper 1). As shown in table 1 of Paper I (for all 13 outflows described in Paper II – VI), the VHP has 6 – 100 times higher N_{H} than the HP, which indicates that the VHP also carries the bulk of the material in the outflows.

Table 5
Analysis Results For the Outflows Seen in SDSS J1042+1646

System	V (km s ⁻¹)	log($U_{\text{H,HP}}$) log	log($N_{\text{H,HP}}$) log(cm ⁻²)	log(n_e) log(cm ⁻³)	log($U_{\text{H,VHP}}$) log	log($N_{\text{H,VHP}}$) log(cm ⁻²)	log(f_V) ^(a)	R pc	\dot{M} (M_{\odot} yr ⁻¹)	Log \dot{E}_k log(erg s ⁻¹)	\dot{E}_k/L_{Edd} %
HE0238 SED:											
1a	-4950	-1.0 ^{+0.2} _{-0.2}	20.4 ^{+0.4} _{-0.4}	3.7 ^{+0.2} _{-0.3}	0.4 ^{+0.2} _{-0.1}	22.4 ^{+0.2} _{-0.1}	-3.4 ^{+0.5} _{-0.7}	840 ⁺⁵⁰⁰ ₋₃₀₀	2800 ⁺²⁰⁰ ₋₈₀₀	46.4 ^{+0.1} _{-0.1}	10 ⁺³ ₋₂
1b	-5750	-0.9 ^{+0.2} _{-0.2}	20.5 ^{+0.4} _{-0.3}	3.8 ^{+0.2} _{-0.3}	0.5 ^{+0.2} _{-0.2}	22.5 ^{+0.3} _{-0.2}	-3.4 ^{+0.6} _{-0.5}	800 ⁺³⁰⁰ ₋₂₀₀	4300 ⁺¹²⁰⁰ ₋₁₅₀₀	46.7 ^{+0.2} _{-0.1}	20 ⁺¹⁴ ₋₄
2	-7500	-0.6 ^{+0.2} _{-0.1}	20.8 ^{+0.3} _{-0.3}	5.8 ^{+0.5} _{-0.3}	0.4 ^{+0.1} _{-0.1}	22.4 ^{+0.1} _{-0.1}	-2.6 ^{+0.4} _{-0.6}	15 ⁺⁸ ₋₈	81 ⁺²⁰ ₋₃₀	45.1 ^{+0.1} _{-0.2}	0.5 ^{+0.2} _{-0.2}
3	-9940	-0.7 ^{+0.1} _{-0.1}	20.7 ^{+0.2} _{-0.2}	—	0.1 ^{+0.1} _{-0.1}	21.5 ^{+0.1} _{-0.1}	-1.6 ^{+0.6} _{-0.3}	—	—	—	—
Transmitted HE0238 SED Emerging From the VHP of OS 2^(b):											
1a	-4950	-0.7 ^{+0.2} _{-0.2}	20.6 ^{+0.3} _{-0.3}	3.7 ^{+0.2} _{-0.3}	1.0 ^{+0.2} _{-0.1}	22.5 ^{+0.3} _{-0.2}	-3.6 ^{+0.4} _{-0.4}	600 ⁺²⁰⁰ ₋₂₀₀	2700 ⁺⁵⁰⁰ ₋₁₀₀	46.4 ^{+0.1} _{-0.1}	8 ⁺² ₋₂
1b	-5750	-0.6 ^{+0.2} _{-0.2}	20.6 ^{+0.3} _{-0.3}	3.8 ^{+0.2} _{-0.3}	1.1 ^{+0.3} _{-0.2}	22.6 ^{+0.4} _{-0.3}	-3.7 ^{+0.5} _{-0.5}	530 ⁺²⁰⁰ ₋₂₀₀	3500 ⁺²⁵⁰⁰ ₋₇₀₀	46.6 ^{+0.2} _{-0.1}	16 ⁺⁸ ₋₃
3	-9940	-0.2 ^{+0.1} _{-0.1}	21.2 ^{+0.1} _{-0.1}	—	1.1 ^{+0.2} _{-0.3}	20.9 ^{+0.3} _{-0.1}	-1.0 ^{+0.3} _{-0.4}	—	—	—	—
Comparison to Other Energetic Outflows:^(c)											
HE0238-1904	-5000	-1.5 ^{+0.6} _{-0.7}	17.6 ^{+0.5} _{-0.1}	3.7 ^{+0.1} _{-0.1}	0.4 ^{+0.1} _{-0.1}	19.6 ^{+0.2} _{-0.1}	-3.9 ^{+0.8} _{-0.7}	3400 ⁺⁹⁰⁰ ₋₂₈₀₀	160 ⁺⁸⁰ ₋₁₅₀	45.7 ^{+0.2} _{-1.2}	4 ⁺² ₋₃
J0831+0354	-10800	-0.2 ^{+0.4} _{-0.5}	22.4 ^{+0.5} _{-0.5}	4.4 ^{+0.3} _{-0.2}	—	—	—	80 ⁺²⁷ ₋₁₈	230 ⁺³³⁰ ₋₁₃₀	45.9 ^{+0.4} _{-0.3}	8 ⁺¹¹ ₋₄

Note. — The bolometric luminosity of SDSS J1042+1646 is $\sim 1.5 \times 10^{47}$ erg s⁻¹.

(a). The volume filling factor of the outflow's high-ionization phase to the very high-ionization phase (see definition in section 6.1.2).

(b). The effect of the transmitted SED is described in section 6.2.

(c). The results of outflows from HE0238-1904 and SDSS J0831+0354 are based on the HE0238 SED with solar metallicity (Arav et al. 2013; Chamberlain et al. 2015).

6.1.2. Volume Filling Factor

Kinematic similarities (both velocity and width centroid) between troughs from the HP and the VHP suggest that these two phases are co-spatial. For each phase (HP or VHP), the volume is proportional to N_H/n_H , and the n_H ratio between the HP and the VHP is given by $U_{H,VHP}/U_{H,HP}$. Therefore, the volume filling factor between the two phases is defined as (see section 8.1 in Arav et al. 2013):

$$f_v \equiv \frac{V_{HP}}{V_{VHP}} = \frac{N_{H,HP}}{N_{H,VHP}} \times \frac{U_{H,HP}}{U_{H,VHP}} \quad (6)$$

where V is the volume of the outflows, and the subscripts HP and VHP denotes the high-ionization phase and very high-ionization phase, respectively. For the outflows in quasar HE0238–1904, the VHP has $\log(U_H)$ 2–3 dexes higher and $\log(N_H)$ 2–2.5 dexes higher than the HP. Therefore, the HP is inferred to have $\log(f_v) \sim -4$ to -6 compared to the VHP. Thus, Arav et al. (2013) reached the conclusion that the VHP carries much more material than the HP and is closer to the situation seen in X-ray warm absorbers (e.g., Netzer et al. 2003; Gabel et al. 2005). We show the f_v values for the outflows in SDSS J1042+1646 in table 5.

6.1.3. Comparisons with Warm Absorbers

In our case, two ionization-phase solutions are sufficient for fitting all the observed outflow features, but it does not exclude more ionization phases. As shown in X-ray warm absorber studies, AGN outflows can span up to 5 orders of magnitude in ionization parameter, i.e., $-1 < \log(\xi) < 4$ (Steenbrugge et al. 2003; Costantini et al. 2007; Holczer et al. 2007; McKernan et al. 2007; Behar 2009), where ξ is the X-ray ionization parameter and for the HE0238 SED, $\log(U_H) = \log(\xi) - 1.3$. Moreover, studies in X-ray invoked a continuous distribution of N_H as a function of ξ (Holczer et al. 2007). The observed absorption features in SDSS J1042+1646 are well fitted with just two ionization phases. However, future sensitive X-ray spectroscopy with observatories such as *Athena* (Barcons et al. 2017) may reveal additional higher-ionization phases and/or the necessity of a continuous distribution of N_H as a function of U_H .

6.2. “Shading Effect” of Different Outflow Systems

Since we have multiple outflow systems along the line of sight at different distances, the inner outflows would absorb photons from the central AGN and could change the SED incident on the outer outflows. This is called the “Shading Effect” (Sun et al. 2017) and here we quantify its effect on our derived photoionization solutions. We show our results when the outflow is directly exposed to the HE0238 SED in the first part of table 5. Outflow S2 has a smaller R compared to the other systems, and its high N_H could significantly affect the SED seen by other outflows. Therefore, we test the shading covered by S2 here and compare it to the original results using the unshaded HE0238 SED.

Our model predicts that S2 has two ionization phases. We input the HE0238 SED and calculate the transmitted SED after passing through S2’s VHP and HP to get $SED_{Tran,VHP}$ and $SED_{Tran,HP}$, respectively. We show

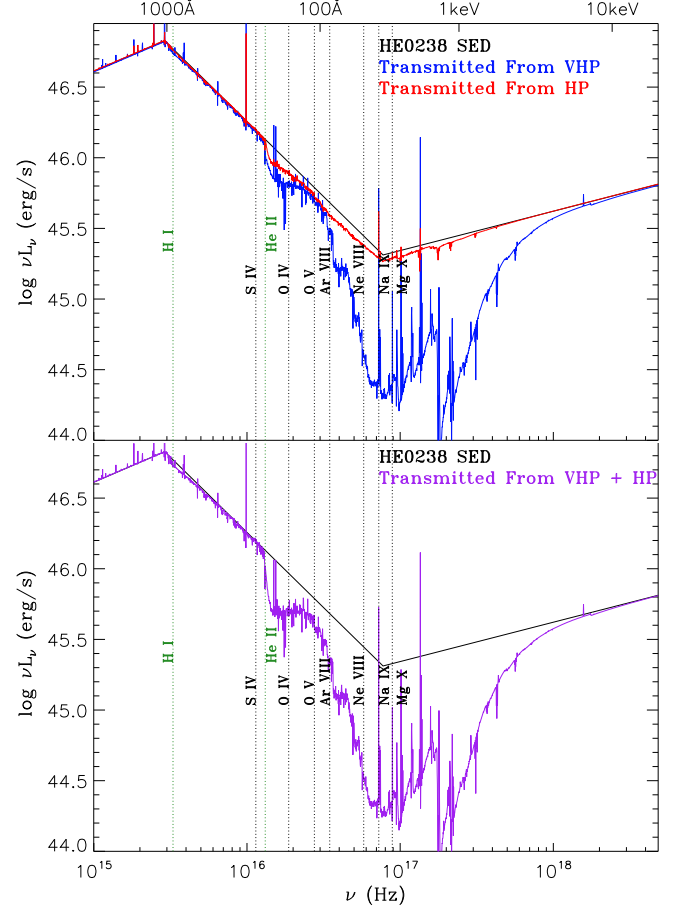


Figure 12. Comparison of the transmitted SEDs (in blue solid lines) to HE0238 SED (in black solid lines). **Top:** We show the transmitted SED emerging from the very high- and high-ionization phase of outflow S2 as blue and red lines, respectively. **Bottom:** We show the transmitted SED emerging from the high-ionization phase of outflow S2 when it is illuminated by $SED_{Tran,VHP}$. In both plots, we indicate the location of the ionization potentials of the main species by the vertical dotted lines. See detailed discussions in section 6.2.

these two transmitted SEDs in the top panel of figure 12 as blue and red lines, respectively. The unshaded HE0238 SED is plotted as the solid black line. The $SED_{Tran,VHP}$ shows a reduction of flux ~ 0.3 dex near the He II edge; and further reduction of flux ~ 1 dex from 100 eV to 1 keV, which is mainly caused by metal absorptions. The $SED_{Tran,HP}$ has a minimal reduction while the largest change is ~ 0.1 dex near the He II edge. To check the total “Shading Effect”, we test the scenario where $SED_{Tran,VHP}$ is incident on the HP of S2. As shown in the bottom panel of figure 12, considering the shading from both phases (purple lines) only affects the SED by an additional 10% compared to the $SED_{Tran,VHP}$ (blue lines in the top panel).

We use these transmitted SEDs as the input SEDs to generate new grids of models with Cloudy. Based on these models and the same method reported in section 4, we find new photoionization solutions for the shaded systems S1a, S1b, and S3. We then calculate new Q_H values using the transmitted SEDs and calculate the outflows’ R , and energetics accordingly [see equations (1), (4), (5)]. We compare these solutions to the un-shaded results in table 5, where the second part of the table is

for the photoionization solutions from SED_{Tran.VHP}. We find that when considering the “Shading Effect” with the SED_{Tran.VHP}, we get a larger $\log(U_H)$ by $\sim 0.3 - 1.0$ dex and a larger $\log(N_H)$ by $\sim 0.1 - 0.5$ dex. This is because the shading of S2 decreases the amount of hydrogen ionizing photons, so a higher U_H is needed to keep a similar ionization state as the unshaded case. The new U_H and N_H values lead to a decrease of ~ 0.1 dex in R , \dot{M} and \dot{E}_k .

6.3. AGN Feedback Effects and Global Covering Factor

As shown in section 1, significant AGN feedback typically requires high \dot{E}_k , where Γ_{Edd} is at least 0.5 (Hopkins & Elvis 2010) or 5% (Scannapieco & Oh 2004). Equations (4) and (5) show that \dot{M} and \dot{E}_k are linearly dependent on the solid angle subtended by the outflows around the source ($4\pi\Omega$). Since there are no direct spectroscopic determinations for Ω , the common approach is to use the detection frequency of outflows in surveys as a proxy. In SDSS J1042+1646, the most energetic outflow is S1b. Based on our analysis results, \dot{M} and \dot{E}_k are given by:

$$\dot{M} \simeq \Omega \times 8600 M_\odot \text{ yr}^{-1} \quad (7)$$

$$\dot{E}_k \simeq \Omega \times 2.5 \times 10^{47} \text{ erg s}^{-1} \quad (8)$$

Multiple surveys have been done to find that C IV BALs appear in approximately 20% of all quasars (e.g., Hewett & Foltz 2003; Dai et al. 2008, 2012; Gibson et al. 2009; Allen et al. 2011). The outflows reported here are consistent with C IV BALs since we observed absorption troughs from O IV $\lambda 787.71$ which has a similar IP to C IV $\lambda 1548.19$. Moreover, the populations of C IV and O IV are similar over a broad range of U_H (see figure 12 in Muza-hid et al. 2013). Also, using the classification scheme in Paper I and the widths of their Ne VIII absorption trough widths in table 2, all of the outflows here are BALs except for S3 which is a mini-BAL. Therefore, Ω of these outflows should be similar to that assumed for C IV BAL outflows. Thus, we adopt an $\Omega = 0.2$ and this lead to $\dot{M} = 4300 M_\odot \text{ yr}^{-1}$ and $\dot{E}_k = 10^{46.7} \text{ erg s}^{-1}$ for outflow S1b. These are the largest \dot{M} and \dot{E}_k reported for quasar outflows to date.

The former records are $\dot{M} \sim 3500 M_\odot \text{ yr}^{-1}$ (Maiolino et al. 2012) and $\dot{E}_k \sim 10^{45.9} \text{ erg s}^{-1}$ (Chamberlain et al. 2015). Moreover, S1b has a $\dot{E}_k \sim 20\%$ of its L_{Edd} . With this high Γ_{Edd} , S1b can be the dominate sources of energy for AGN feedback in the host galaxy of SDSS J1042+1646 (Scannapieco & Oh 2004).

Similarly, for component 1a, this yields $R = 840^{+500}_{-300}$ pc, $\dot{M} = 2800^{+200}_{-800} M_\odot \text{ yr}^{-1}$ and $\log(\dot{E}_k) = 46.4^{+0.1}_{-0.1} \text{ erg s}^{-1}$. Combining S1a and S1b, outflow S1 has an \dot{E}_k close to $10^{47.0} \text{ erg s}^{-1}$ and Γ_{Edd} close to 30%.

6.4. Effects of the Super Solar Metallicity

AGN outflows can exhibit super solar metallicity (SSM) (e.g., Arav et al. 2007; Gabel et al. 2006). Paper V discusses the quantitative effects of SSM on the inferred parameters for outflows observed in the EUV500.

Unlike the case shown in Paper V, the photoionization solutions of S1, S2, and S3 in SDSS J1042+1646 are consistent with solar metallicity. To estimate the effects of possible SSM on S1, S2, and S3, we follow approach from Paper V and compute the analysis results for two metallicity values: solar (Z_\odot) and 4.7 times solar ($4.7Z_\odot$). For outflow system 1 and 2, the results based on $4.7Z_\odot$ leads to a decrease of distance by up to 30% and decreases of \dot{M} and \dot{E}_k by up to a factor of 6. However, the goodness of the fit (determined by their χ^2) for all models is comparable, so the fits cannot provide a metallicity constraint.

7. SUMMARY

In this paper, we presented the analysis of HST/COS spectra for the quasar outflows seen in SDSS J1042+1646 in the EUV500 (500 – 1050 Å rest-frame) region. The results are summarized as follows:

1. A total of five outflow systems are identified (S1 – S4, where S1 has two components: S1a and S1b). From these outflows, we observed absorption troughs from both high-ionization species, e.g., O IV, and S IV, and very high-ionization species, e.g., Ar VIII, Ne VIII, Na IX, and Mg X. Four out of the five outflows are defined as BAL outflows while the other (S3) is a mini-BAL outflow (see section 3.2).
2. We developed the Synthetic Spectral Simulation method to efficiently fit the multitude of observed troughs with a three-dimensional model grid in the parameter space of U_H , N_H , and n_e . This method is especially powerful when handling blended absorption troughs from many EUV500 species (>70), and intervening absorption troughs (see section 3.3).
3. The appearance of the very high-ionization species necessitates at least two-ionization phase solutions for the observed outflows. Combining with previous studies, we suggest that all HiBALs have very high-ionization phases, which are almost exclusively accessible with EUV500 observations from HST (see section 4).
4. With determining n_e from density sensitive transitions, we found the distances and energetics for 3 out of the 5 outflows. Outflow system 1 has \dot{E}_k close to $10^{47.0} \text{ erg s}^{-1}$, which is the most energetic outflow observed in quasars to date. Moreover, this leads to an \dot{E}_k/L_{Edd} close to 30%, which makes it a good candidate for being the agent of quasar-mode AGN feedback (see section 5).
5. When we take into account the attenuation of ionizing flux by interior outflow systems, we find a decrease of ~ 0.1 dex in R , \dot{M} and \dot{E}_k (see section 6.2).

X.X., N.A., and T.M acknowledge support from NSF grant AST 1413319, as well as NASA STScI grants GO 14777, 14242, 14054, and 14176, and NASA ADAP 48020.

Based on observations made with the NASA/ESA Hubble Space Telescope, obtained from the data archive at the Space Telescope Science Institute. STScI is operated by the Association of Universities for Research in Astronomy, Inc. under NASA contract NAS5-26555.

CHIANTI is a collaborative project involving George Mason University (USA), the University of Michigan

(USA) and the University of Cambridge (UK).

REFERENCES

- Allen K. W., 1977, *asqu.book*
- Allen, J. T., Hewett, P. C., Maddox, N., Richards, G. T., & Belokurov, V. 2011, *MNRAS*, 410, 860
- Anglés-Alcázar, D., Davé, R., Faucher-Giguère, C.-A., Özel, F., & Hopkins, P. F. 2017, *MNRAS*, 464, 2840
- Arav, N., Korista, K. T., de Kool, M., Junkkarinen, V. T., & Begelman, M. C. 1999, *ApJ*, 516, 27
- Arav, N., de Kool, M., Korista, K. T., et al. 2001, *ApJ*, 561, 118
- Arav, N., Kaastra, J., Kriss, G. A., et al. 2005, *ApJ*, 620, 665
- Arav, N., Gabel, J. R., Korista, K. T., et al. 2007, *ApJ*, 658, 829
- Arav, N., Moe, M., Costantini, E., et al. 2008, *ApJ*, 681, 954-964
- Arav, N., Edmonds, D., Borguet, B., et al. 2012, *A&A*, 544, AA33
- Arav, N., Borguet, B., Chamberlain, C., Edmonds, D., & Danforth, C. 2013, *MNRAS*, 436, 3286
- Arav N., Chamberlain, C., Kriss, G. A., et al., 2015, *A&A*, 577, A37
- Arav, N., Liu, G., Xu, X., et al. 2018, *ApJ*, 857, 60
- Arav, N., Xu, X., Miller, T. R., et al. 2020, *ApJS*, in press
- Ballero, S. K., Matteucci, F., Ciotti, L., Calura, F., & Padovani, P. 2008, *A&A*, 478, 335
- Baskin, A., & Laor, A. 2012, *MNRAS*, 426, 1144
- Bahk, H., Woo, J.-H., & Park, D. 2019, *ApJ*, 875, 50
- Barcons, X., Barret, D., Decourchelle, A., et al. 2017, *AN*, 338, 153
- Borguet, B. C. J., Edmonds, D., Arav, N., Dunn, J., & Kriss, G. A. 2012a, *ApJ*, 751, 107
- Borguet, B. C. J., Edmonds, D., Arav, N., Benn, C., & Chamberlain, C. 2012, *ApJ*, 758, 69
- Borguet, B. C. J., Arav, N., Edmonds, D., Chamberlain, C., & Benn, C. 2013, *ApJ*, 762, 49
- Boroson, T. A., & Meyers, K. A. 1992, *ApJ*, 397, 442
- Becker, R. H., White, R. L., Gregg, M. D., et al. 2000, *ApJ*, 538, 72
- Chamberlain, C., & Arav, N. 2015, *MNRAS*, 454, 675
- Chamberlain, C., Arav, N., & Benn, C. 2015, *MNRAS*, 450, 1085
- Choi, E., Somerville, R. S., Ostriker, J. P., Naab, T., & Hirschmann, M. 2018, *ApJ*, 866, 91
- Ciotti, L., Pellegrini, S., Negri, A., & Ostriker, J. P. 2017, *ApJ*, 835, 15
- Costantini, E., Kaastra, J. S., Arav, N., et al. 2007, *A&A*, 461, 121
- Capellupo, D. M., Hamann, F., Shields, J. C., Rodríguez Hidalgo, P., & Barlow, T. A. 2012, *MNRAS*, 422, 3249
- Capellupo, D. M., Hamann, F., & Barlow, T. A. 2014, *MNRAS*, 444, 1893
- Capellupo, D. M., Hamann, F., Herbst, H., et al. 2017, *MNRAS*, 469, 323
- de Kool, M., Arav, N., Becker, R. H., et al. 2001, *ApJ*, 548, 609
- de Kool, M., Becker, R. H., Gregg, M. D., White, R. L., & Arav, N. 2002, *ApJ*, 567, 58
- de Kool, M., Korista, K. T., & Arav, N. 2002, *ApJ*, 580, 54
- Dai, X., Shankar, F., & Sivakoff, G. R. 2008, *ApJ*, 672, 108-114
- Dai, X., Shankar, F., & Sivakoff, G. R. 2012, *ApJ*, 757, 180
- Di Matteo, T., Springel, V., & Hernquist, L. 2005, *Nature*, 433, 604
- de Kool M., Korista K. T., Arav N., 2002, *ApJ*, 580, 54
- Doyle, J. G., Dufton, P. L., Keenan, F. P., & Kingston, A. E. 1983, *Sol. Phys.*, 89, 243
- Dunn, J. P., Crenshaw, D. M., Kraemer, S. B., & Trippe, M. L. 2010, *ApJ*, 713, 900
- Edmonds, D., Borguet, B., Arav, N., et al. 2011, *ApJ*, 739, 7
- Behar, E. 2009, *ApJ*, 703, 1346
- Behar, E., Peretz, U., Kriss, G. A., et al. 2017, *A&A*, 601, A17
- Ferland, G. J., Chatzikos, M., Guzman, F., et al. 2017, *RMxAA*, 53, 385
- Faucher-Giguère, C.-A., Quataert, E., & Murray, N. 2012, *MNRAS*, 420, 1347
- Finn, C. W., Morris, S. L., Crighton, N. H. M., et al. 2014, *MNRAS*, 440, 3317
- Ferrarese, L., & Merritt, D. 2000, *ApJ*, 539, L9
- Fischer, C. F., Tachiev, G., & Irimia, A. 2006, *Atomic Data and Nuclear Data*, 92, 607 – 812
- Fox A., James B., Roman-Duval J., Rafelski M., Sonnentrucker P., 2018, *cos..rept*
- Grevesse, N., Asplund, M., Sauval, A. J., & Scott, P. 2010, *Ap&SS*, 328, 179
- Gabel, J. R., Kraemer, S. B., Crenshaw, D. M., et al. 2005, *ApJ*, 631, 741
- Gabel, J. R., Arav, N., & Kim, T.-S. 2006, *ApJ*, 646, 742
- Ganguly, R., & Brotherton, M. S. 2008, *ApJ*, 672, 102-107
- Gibson, R. R., Brandt, W. N., Schneider, D. P., & Gallagher, S. C. 2008, *ApJ*, 675, 985
- Gibson, R. R., Jiang, L., Brandt, W. N., et al. 2009, *ApJ*, 692, 758
- Gibson, R. R., Brandt, W. N., Gallagher, S. C., Hewett, P. C., & Schneider, D. P. 2010, *ApJ*, 713, 220
- Grier, C. J., Hall, P. B., Brandt, W. N., et al. 2015, *ApJ*, 806, 111.
- Green, James C., Froning, Cynthia S., Osterman, Steve, et al., 2012, *ApJ*, 744, 60
- Hall, P. B., Anderson, S. F., Strauss, M. A., et al. 2002, *ApJS*, 141, 267
- Hamann, F. 1998, *ApJ*, 500, 798
- Hamann, F. W., Barlow, T. A., Chaffee, F. C., Foltz, C. B., & Weymann, R. J. 2001, *ApJ*, 550, 142
- Hamann, F., Herbst, H., Paris, I., & Capellupo, D. 2019, *MNRAS*, 483, 1808
- Hewett, P. C., & Foltz, C. B. 2003, *AJ*, 125, 1784
- Hopkins, P. F., & Elvis, M. 2010, *MNRAS*, 401, 7
- Hopkins, P. F., Younger, J. D., Hayward, C. C., Narayanan, D., & Hernquist, L. 2010, *MNRAS*, 402, 1693
- Hopkins, P. F., Torrey, P., Faucher-Giguère, C.-A., Quataert, E., & Murray, N. 2016, *MNRAS*, 458, 816
- Hopkins, P. F., Hernquist, L., Cox, T. J., et al. 2005, *ApJ*, 630, 716
- Hopkins, P. F., Richards, G. T., & Hernquist, L. 2007, *ApJ*, 654, 731
- Holczer, T., Behar, E., & Kaspi, S. 2007, *ApJ*, 663, 799
- Korista, K. T., Weymann, R. J., Morris, S. L., et al. 1992, *ApJ*, 401, 529
- Korista, K. T., Bautista, M. A., Arav, N., et al. 2008, *ApJ*, 688, 108-115
- Keenan, F. P., Warren, G. A., Doyle, J. G., Berrington, K. A., & Kingston, A. E. 1994, *Sol. Phys.*, 150, 61
- King, A. 2003, *ApJ*, 596, L27
- Kramida, A., Ralchenko, Yu., Reader, J., and NIST ASD Team (2018). NIST Atomic Spectra Database (ver. 5.6.1), [Online]. Available: <https://physics.nist.gov/asd> [2019, April 26]. National Institute of Standards and Technology, Gaithersburg, MD. DOI: <https://doi.org/10.18434/T4W30F>
- Landi, E., Young, P. R., Dere, K. P., Del Zanna, G., & Mason, H. E. 2013, *ApJ*, 763, 86
- Leighly, K. M., Hamann, F., Casebeer, D. A., & Grupe, D. 2009, *ApJ*, 701, 176
- Leighly, K. M., Dietrich, M., & Barber, S. 2011, *ApJ*, 728, 94
- Leighly, K. M., Terndrup, D. M., Gallagher, S. C., Richards, G. T., & Dietrich, M. 2018, *ApJ*, 866, 7
- Leighly K. M., Terndrup, D. M., Lucy, A. B, et al., 2019, *ApJ*, 879, 27
- Maolino, R., Gallerani, S., Neri, R., et al. 2012, *MNRAS*, 425, L66
- McCarthy, I. G., Schaye, J., Ponman, T. J., et al. 2010, *MNRAS*, 406, 822
- Miller, T. R., Arav, N., Xu, X., et al. 2018, *ApJ*, 865, 90
- Miller, T. R., Arav, N., Xu, X., et al. 2020, *ApJS*, in press
- Miller, T. R., Arav, N., Xu, X., et al. 2020, *ApJS*, in press
- Miller, T. R., Arav, N., Xu, X., et al. 2020, in preparation
- Moll, R., Schindler, S., Domainko, W., et al. 2007, *A&A*, 463, 513
- McKernan, B., Yaqoob, T., & Reynolds, C. S. 2007, *MNRAS*, 379, 1359
- Moe M., Arav N., Bautista M. A., Korista K. T., 2009, *ApJ*, 706, 525
- Muzahid, S., Srianand, R., Arav, N., Savage, B. D., & Narayanan, A. 2013, *MNRAS*, 431, 2885
- Netzer, H., Kaspi, S., Behar, E., et al. 2003, *ApJ*, 599, 933
- Ostriker, J. P., Choi, E., Ciotti, L., Novak, G. S., & Proga, D. 2010, *ApJ*, 722, 642
- O'Shea, E., O'Neill, T., Keenan, F. P., & Doyle, J. G. 2000, *Sol. Phys.*, 196, 321
- Park, D., Barth, A. J., Woo, J.-H., et al. 2017, *ApJ*, 839, 93

- Peterson, B. M., Ferrarese, L., Gilbert, K. M., et al. 2004, *ApJ*, 613, 682
- Reichard, T. A., Richards, G. T., Schneider, D. P., et al. 2003, *AJ*, 125, 1711
- Savage, B. D., & Sembach, K. R. 1991, *ApJ*, 379, 245
- Scannapieco, E., & Oh, S. P. 2004, *ApJ*, 608, 62
- Silva, C. V., Uttley, P., & Costantini, E. 2016, *A&A*, 596, A79
- Silk, J., & Rees, M. J. 1998, *A&A*, 331, L1
- Soker, N., & Meiron, Y. 2011, *MNRAS*, 411, 1803
- Schlafly, E. F., & Finkbeiner, D. P. 2011, *ApJ*, 737, 103
- Sun, L., Zhou, H., Ji, T., et al. 2017, *ApJ*, 838, 88
- Steenbrugge, K. C., Kaastra, J. S., de Vries, C. P., & Edelson, R. 2003, *A&A*, 402, 477
- Taylor, P., & Kobayashi, C. 2015, *MNRAS*, 452, L59
- Trump, J. R., Hall, P. B., Reichard, T. A., et al. 2006, *ApJS*, 165, 1
- Telfer, R. C., Kriss, G. A., Zheng, W., Davidsen, A. F., & Green, R. F. 1998, *ApJ*, 509, 132
- Telfer, R. C., Kriss, G. A., Zheng, W., Davidsen, A. F., & Tytler, D. 2002, *ApJ*, 579, 500
- Tolea, A., Krolik, J. H., & Tsvetanov, Z. 2002, *ApJ*, 578, L31
- Verner D. A., Verner E. M., Ferland G. J., 1996, *ADNDT*, 64, 1
- Varsavsky, C. M. 1961, *ApJS*, 6, 75
- Voit, G. M., Weymann, R. J., & Korista, K. T. 1993, *ApJ*, 413, 95
- Weymann, R. J., Morris, S. L., Foltz, C. B., & Hewett, P. C. 1991, *ApJ*, 373, 23
- Wright, E. L. 2006, *PASP*, 118, 1711
- Xu, X., Arav, N., Miller, T., & Benn, C. 2018, *ApJ*, 858, 39
- Xu X., Arav N., Miller T., Benn C., 2019a, *ApJ*, 876, 105
- Xu, X., Arav, N., & Miller, T. 2020, *ApJS*, in press
- Xu, X., Arav, N., & Miller, T. 2020, *ApJS*, in press
- Xu, X., Arav, N., & Miller, T. 2020, *ApJS*, in press